Mapping the Conformational Landscape of a Dynamic Enzyme by Multitemperature and XFEL Crystallography

Daniel A. Keedy[1*], Lillian R. Kenner[1*], Matthew Warkentin[2*], Rahel A. Woldeyes[1*], Jesse B. Hopkins[2], Michael C. Thompson[1], Aaron S. Brewster[3], Andrew H. Van Benschoten[1], Elizabeth L. Baxter[4], Monarin Uervirojnangkoorn[5,6], Scott E. McPhillips[4], Jinhu Song[4], Roberto Alonso-Mori[7], James M. Holton[3,4,8], William I. Weis[5,9,10], Axel T. Brunger[5,6,9,10], S. Michael Soltis[4], Henrik Lemke[7], Ana Gonzalez[4], Nicholas K. Sauter[3], Aina E. Cohen[4], Henry van den Bedem[4#], Robert E. Thorne[2#], James S. Fraser[1#]

1 - Dept. of Bioengineering and Therapeutic Sciences, University of California, San Francisco, San Francisco, CA 94158
2 - Physics Dept., Cornell University, Ithaca, NY 14853
3 - Physical Biosciences Division, Lawrence Berkeley National Laboratory, Berkeley, CA 94720
4 - Stanford Synchrotron Radiation Lightsource, SLAC National Accelerator Laboratory, Menlo Park, CA 94025
5 - Dept. of Molecular and Cellular Physiology, Stanford University, Stanford, CA 94305
6 - Howard Hughes Medical Institute, Stanford University, Stanford, CA 94305
7 - Linac Coherent Light Source, SLAC National Accelerator Laboratory, Menlo Park, CA 94025
8 - Dept. of Biochemistry and Biophysics, University of California, San Francisco, San Francisco, CA 94158
9 - Dept. of Structural Biology, Stanford University, Stanford, CA 94305
10 - Dept. of Photon Sciences, SLAC National Accelerator Laboratory, Menlo Park, CA 94025

Author contributions:

Prepared Samples: LRK, MW, JSF
Collected XFEL Data: LRK, RAW, ASB, AHVB, ELB, SEM, JS, RAM, SMS, HL, AG, AEC, HvdB, JSF
Collected Synchrotron data: MW, JBH, HvdB, JSF
Processed Data: RAW, ASB, NKS, MCT, AHVB, DAK, MU, JMH, WIW, ATB, AG
Analyzed Data: DAK, RAW, MCT, HvdB, RET, JSF
Wrote Paper: DAK, RAW, HvdB, RET, JSF
Edited Paper: All authors

*equal contributions
#corresponding authors: vdbedem@slac.stanford.edu, ret6@cornell.edu, james.fraser@ucsf.edu

Abstract

Determining the interconverting conformations of dynamic proteins in atomic detail is a major challenge for structural biology. Conformational heterogeneity in the active site of the dynamic enzyme cyclophilin A (CypA) has been previously linked to its catalytic function, but the extent to which the different conformations of these residues are correlated is unclear. Here we compare the conformational ensembles of CypA by multitemperature synchrotron crystallography and fixed-target X-ray free electron laser (XFEL) crystallography. The "diffraction-before-destruction" nature of XFEL experiments provides a radiation-damage-free view of the functionally important alternative conformations of CypA, confirming earlier synchrotron-based results. We monitored the temperature dependences of these alternative conformations with eight synchrotron datasets spanning 100-310 K. Multiconformer models show that many alternative conformations in CypA are populated only at 240 K and above, yet others remain populated or become populated at 180 K and below. These results point to a complex evolution of conformational heterogeneity between 180-240 K that involves both thermal deactivation and solvent-driven arrest of protein motions in the crystal. The lack of a single shared conformational response to temperature within the dynamic active-site network provides evidence for a conformation shuffling model, in which exchange between rotamer states for a large aromatic ring in the middle of the network shifts the conformational ensemble for the other residues in the network. Together, our multitemperature analyses and XFEL data motivate a new generation of temperature- and time-resolved experiments to structurally characterize the dynamic underpinnings of protein function.

Introduction

Current structural biology methods provide only incomplete pictures of how proteins interconvert between distinct conformations (Motlagh et al., 2014; van den Bedem and Fraser, 2015). Although X-ray crystallography reveals atomic coordinates with relatively high accuracy and precision, the resulting electron density maps contain contributions from multiple alternative conformations reflecting the ensemble average of 10^6-10^{15} copies of the protein in one crystal (Rejto and Freer, 1996; Smith et al., 1986; Woldeyes et al., 2014). At high resolution, it is often possible to detect and discretely model these alternative conformations (Burnley et al., 2012; Davis et al., 2006; Lang et al., 2010; van den Bedem et al., 2009). Structural characterization of alternative conformations by X-ray crystallography can complement NMR (Baldwin and Kay, 2009; Fenwick et al., 2014) and computational simulations (Dror et al., 2012; Ollikainen et al., 2013) in defining the structural basis of protein dynamics and ultimately in linking dynamics to function (Henzler-Wildman and Kern, 2007).

However, more than 95% of crystal structures are determined at cryogenic temperatures (~100 K) to reduce radiation damage by minimizing diffusion of reactive intermediates and chemical-damage-induced structural relaxations (Garman, 2010; Holton, 2009; Warkentin et al., 2013). Unfortunately, cryocooling can modify mainchain and sidechain conformational distributions throughout the protein, including at active sites and distal regions important for allosteric function (Fraser et al., 2011; Halle, 2004; Keedy et al., 2014). Recent studies have instead used room-temperature data collection to reveal a multitude of previously "hidden" alternative conformations that are not evident at cryogenic temperatures, many of which have important ramifications for determining molecular mechanisms (Deis et al., 2014; Fraser et al., 2009; Fukuda and Inoue, 2015; Keedy et al., 2014; van den Bedem et al., 2013).

Between these temperature extremes, protein conformational heterogeneity changes in complex ways. Previous studies using a wide variety of biophysical probes including NMR, X-ray crystallography, and neutron scattering have revealed a change in the character of conformational heterogeneity and/or protein dynamics around 180-220 K (Doster, 2010; Frauenfelder et al., 2009; Lewandowski et al., 2015; Ringe and Petsko, 2003); however, the molecular origins of this "glass" or "dynamical" transition remain incompletely understood. Classic work has examined the temperature dependence of protein conformational heterogeneity across individual X-ray structures determined at temperatures from ~80-320 K (Frauenfelder et al., 1987; Frauenfelder et al., 1979; Tilton et al., 1992). These studies used atomic B-factors as a proxy for conformational heterogeneity and identified a global inflection point around 180-220 K. This inflection point was interpreted in terms of a transition driven by dynamical arrest of the coupled hydration layer-protein system (Doster et al., 1989; Frauenfelder et al., 2009; Frauenfelder et al., 1987; Tilton et al., 1992). In contrast, solution NMR studies of ps-ns timescale methyl sidechain order parameters showed heterogeneous changes in motional amplitudes at temperatures between 288 K and 346 K. Thermal deactivation of these motions was suggested to predict a transition near 200 K without invoking solvent arrest (Lee and Wand, 2001). Recent solid-state NMR (ssNMR) experiments suggest that protein

87 motions are coupled to solvent, and that three transitions at ~195, 220, and 250 K mark the onset of distinct
88 classes of motions as temperature increases (Lewandowski et al., 2015). Unfortunately, these studies either used
89 globally averaged data (as with ssNMR or neutron scattering) or imprecisely define atomic-level models of
90 conformational heterogeneity (as with B-factors in X-ray crystallography or NMR order parameters), thus
91 preventing an all-atom understanding of the complex temperature response of protein crystals.
92
93 New crystallographic and computational techniques now enable a more detailed investigation of the temperature
94 dependence of protein conformational heterogeneity at the atomic level. First, the program Ringer (Lang et al.,
95 2014; Lang et al., 2010) evaluates low-level electron density traditionally considered noise to uncover statistically
96 significant "hidden" alternative conformations, which may become populated or depopulated as a function of
97 temperature. Second, multiconformer models with explicit alternative conformations of both backbone and
98 sidechain atoms, as created by manual building or the program qFit (van den Bedem et al., 2013; van den Bedem
99 et al., 2009), can account for non-harmonic motions across separate energy wells (encoded by discrete alternative
100 conformations with distinct occupancies and coordinates) and harmonic motions within energy wells (encoded by
101 B-factors). Third, crystallographic order parameters (S^2) weight these harmonic and non-harmonic contributions
102 in a single metric that quantifies the disorder of each residue in a multiconformer model, allowing direct
103 comparison with NMR-determined order parameters (Fenwick et al., 2014). Finally, methodological advances
104 based on the physics of ice formation have enabled variable-temperature crystallographic data collection at
105 temperatures between 300 K and 100 K with modest or no use of potentially conformation-perturbing
106 cryoprotectants (Warkentin et al., 2012; Warkentin and Thorne, 2009). Together, these methods overcome many
107 of the limitations of previous X-ray-based approaches, and will contribute to an integrated view of how protein
108 conformational heterogeneity and dynamics evolve with temperature.
109
110 The human proline isomerase cyclophilin A (CypA) is an excellent model system for deploying these tools to
111 study the structural basis of functional conformational dynamics and, in particular, to use temperature to
112 understand the extent of correlated motions during an enzyme's catalytic cycle. Previous NMR relaxation data for
113 CypA (Eisenmesser et al., 2002; Eisenmesser et al., 2005) indicated a single common exchange process, both in
114 the apo state and during catalysis, for a network of dynamic residues extending from the core to the active site.
115 Room-temperature crystallography later suggested the precise alternative conformations that collectively
116 interconvert during catalysis (Fraser et al., 2009). However, subsequent NMR relaxation experiments of mutants
117 designed to perturb the dynamics suggested that multiple exchange processes occur within this network (Schlegel
118 et al., 2009). Here, we analyze multitemperature synchrotron experiments to examine the temperature-dependent
119 conformational heterogeneity of CypA. Additionally, we report X-ray free electron laser (XFEL) data, which are
120 free of conventional radiation damage (Kern et al., 2014; Spence et al., 2012), to validate previous connections
121 between alternative conformations determined by synchrotron crystallography and NMR experiments performed
122 in solution (Eisenmesser et al., 2005; Fraser et al., 2009). Our analysis shows that the temperature dependence of

alternative protein conformations is heterogeneous and that the character of this heterogeneity bridges previous models for protein dynamical transitions. Our results also suggest new ways to use variable temperature with both synchrotron and XFEL crystallography to probe the dynamic underpinnings of protein function.

Results

Multitemperature X-ray Datasets Reveal Modulated Conformational Ensembles of CypA

To probe the conformational landscape of CypA, we collected eight high-resolution (1.34-1.58 Å) synchrotron crystallographic datasets across a wide range of temperatures from 100-310 K (**Table 1**) with no added cryoprotectants. For each dataset, we initially refined single-conformer models. Although the single-conformer models are very similar to each other, the accompanying electron density maps reveal differences throughout the protein. In the active-site network, the mFo-DFc difference electron density maps are relatively featureless below 200 K, suggesting that a single conformation is a valid fit below this temperature. By contrast, positive and negative mFo-DFc peaks become gradually more prevalent as temperature increases above 200 K, suggesting that multiple conformations are increasingly required to explain the data as temperature increases (**Table 1 – Figure S1**).

We monitored the shift from single-conformation to multiple conformations both visually (**Figure 1 A,B**) and using the automated electron-density scanning program Ringer (**Figure 1 C,D**). Briefly, Ringer identifies alternative conformations at low levels of electron density by evaluating the density value for the γ atom at each possible position about the χ1 dihedral angle, given a fixed mainchain conformation (Lang et al., 2014; Lang et al., 2010). We focused on two residues, Ser99 and Leu98, which are key markers of the conformational exchange by NMR (Eisenmesser et al., 2002; Eisenmesser et al., 2005) and were implicated in our previous room-temperature X-ray and mutagenesis experiments (Fraser et al., 2009). For both Ser99 (**Figure 1 A**) and Leu98 (**Figure 1 B**), a dominant peak is evident at all temperatures. The reduced height of this peak as temperature increases is accompanied by the increase in a secondary peak corresponding to the electron density of the minor conformation. To quantify this trend, we computed correlation coefficients between the electron density vs. dihedral angle curves for each residue (**Figure 1 C,D**). Pairs of curves for similar temperatures have higher correlations than those for different temperatures. In particular, pairs of curves for temperatures that span the low-temperature (100-180 K) and high-temperature (240-310 K) regimes are more poorly correlated than are curves from the same temperature regime. The dynamical transitions observed in previous studies (Doster, 2010; Lee and Wand, 2001; Lewandowski et al., 2015; Ringe and Petsko, 2003; Schiro et al., 2015) generally occur between these two temperature regimes.

To ground this conformational redistribution in all-atom detail, we built a multiconformer model with qFit (van

159 den Bedem et al., 2013; van den Bedem et al., 2009) for each multitemperature dataset. We then finalized the
160 model by manually editing alternative conformations and refining to convergence, resulting in models that were
161 improved relative to the single-conformer models (**Table 2**, **Movie 1**). At 180 K and below, the active-site
162 network is best modeled as a single state, with electron density corresponding to ordered water molecules clearly
163 evident adjacent to Phe113 (**Figure 2**, top row). At 240 K and above, by contrast, multiple conformations provide
164 a better explanation of the data. Interestingly, some partial-occupancy water molecules are still present and likely
165 co-occur with the major conformations (**Figure 2**, middle and bottom rows). Met61 appears to populate additional
166 conformations above 180 K, although it is difficult to precisely define changes in its conformational ensemble as
167 temperature increases. This residue bridges Phe113 and the catalytic residue Arg55 via steric contacts between
168 alternative conformations in both directions, emphasizing the importance of modeling multiple conformations in
169 all-atom detail for understanding inter-residue coupling.
170
171 *XFEL Data Confirm Conformational Heterogeneity in Synchrotron Data Is Not Due to Radiation Damage*
172
173 Quantifying radiation damage versus exposure dose (**Table 1 – Figure Supplement 2**) and limiting exposure
174 dose per dataset ensured that the conformational heterogeneity observed in multitemperature synchrotron datasets
175 was not dominated by radiation damage. However, XFELs can generate data that is entirely free from
176 conventional radiation damage by "diffraction before destruction" data collection (Kern et al., 2014; Spence et al.,
177 2012). To compare the distribution of alternative conformations between synchrotron and XFEL data, we
178 collected two ambient-temperature datasets: a 1.75 Å resolution radiation-damage-free dataset using serial
179 femtosecond rotation crystallography (**Table 3**) (Hirata et al., 2014; Schlichting, 2015; Suga et al., 2015) and an
180 additional 1.2 Å resolution synchrotron dataset (**Table 4**). For the XFEL experiment, we collected 1,239
181 individual frames, translating to unique unexposed regions of 71 crystals between each shot (**Movie 2**), and
182 processed them using cctbx.xfel (Hattne et al., 2014) with post-refinement in PRIME (Uervirojnangkoorn et al.,
183 2015). Automated molecular replacement yielded interpretable electron density maps that allowed us to refine a
184 single-conformer structural model with reasonable quality statistics. Electron-density sampling analysis using
185 Ringer and multiconformer refinement using qFit were performed as for the multitemperature synchrotron data.
186
187 In agreement with our previous room-temperature studies (Fraser et al., 2009), the XFEL and synchrotron mFo-
188 DFc difference maps reveal evidence for the rate-limiting alternative conformations extending from the active site
189 into the core of the protein (**Figure 3 A,B**). For example, the backrub-coupled (Davis et al., 2006) rotamer jump
190 of Phe113 is apparent from a large positive mFo-DFc peak in both maps. Alternative conformations for core
191 residue Ser99 are also evident from mFo-DFc peaks (**Figure 3 A,B**) and Ringer electron-density sampling curves
192 (**Figure 3 E**). We did not conclusively observe a secondary peak in the electron density sampling curve
193 corresponding to a discrete alternative conformation of Leu98 (**Figure 3 F**), but that is likely due to the lower
194 resolution of the XFEL dataset. Multiconformer models for both datasets (**Figure 3 C,D**) again feature alternative

conformations across the active-site network and are strongly supported by 2mFo-DFc electron density. These results provide an important positive control on the observation of conformational heterogeneity in our synchrotron studies by establishing that electron density corresponding to the alternative conformations of CypA is not an artifact of radiation damage. The ability of XFEL crystallography to reveal native and functionally important alternative conformations at high resolution may be especially useful for other systems that are presently intractable for room- or variable-temperature synchrotron crystallography due to the small size of available crystals.

Some Regions Feature Conformational Heterogeneity Only At Low Temperatures

Although more conformational heterogeneity is expected with our higher-temperature synchrotron datasets, and is evident in the active site of CypA, cooling can also stabilize new conformations (Halle, 2004). For example, the loop containing residues 79-83 (**Figure 4**, **Movie 3**) exhibits conformational heterogeneity only at cryogenic temperatures. This region is well fit by a single conformation at 240 K and above, but a secondary loop conformation is necessary to explain the electron density at 100, 150, and 180 K. Additionally, the loop is clearly single-state in the highest-resolution (1.2 Å) dataset (**Figure 4 - Figure S1**), demonstrating that the slightly lower resolution of the elevated-temperature datasets does not obscure a secondary conformation.

In the primary conformation, the 79-83 loop is not involved in any mainchain-mainchain hydrogen bonds to the rest of CypA, suggesting that the barrier to forming the secondary conformation does not involve breakage of cooperative secondary-structure-like interactions. The observation of a secondary state for residues 79-83 at 100-180 K, but not at 240-310 K, suggests that it is enthalpically stabilized at lower temperatures (Halle, 2004; Keedy et al., 2014). Consistent with this mechanism, the secondary conformation of the 79-83 loop is accompanied by an ordered, partial-occupancy water molecule (**Figure 4**, top row). This water molecule, which is clearly distinct from the carbonyl oxygen of the primary conformation of Glu81, wedges between the loop and the rest of the protein. The surprising appearance of specific solvent-linked protein conformational heterogeneity exclusively below 240 K emphasizes the complex and heterogeneous changes in protein-solvent energetics that can occur at cryogenic temperatures.

Quantifying Temperature-Dependent Changes in Conformational Heterogeneity

Despite counterexamples such as the 79-83 loop, most residues in CypA, especially in the active site, exhibit increases in discrete conformational heterogeneity above 180 K. To quantify these changes in regions implicated by NMR relaxation experiments, we measured the 2mFo-DFc electron density in the volumes occupied by the alternative conformations of Ser99 and Phe113. In contrast, B-factors, which can model the harmonic motions near any single conformation, are poor proxies for the non-harmonic change between discretely separated

conformations. To quantify the change in minor state occupancy as a function of temperature, we summed the electron density in the volume that is occupied exclusively by the minor conformation, and avoided any voxels that overlap with the van der Waals radii of atoms of the major conformation (**Figure 5 A**). The resulting curves of minor-state electron density vs. temperature have a shallow slope at 180 K and below, but a much steeper slope at 240 K and above (**Figure 5 B,C**). Additionally, the electron density for the XFEL data is consistent with the data collection temperature (273 K) and the overall trends.

However, most residues that populate alternative conformations do not have such easily characterized and separable regions of electron density. To quantify how conformational heterogeneity throughout CypA varies as a function of temperature, we used B-factor-dependent crystallographic order parameters (S^2) (Fenwick et al., 2014). These order parameters include both harmonic contributions, which reflect conformational heterogeneity near one conformation (encoded by B-factors), and non-harmonic contributions, which reflect conformational heterogeneity between multiple discretely separated conformations (encoded by occupancies and displacements in coordinates). Importantly, these order parameters account for both conformational heterogeneity within energy wells, whether it is modeled by B-factors or by subtly different alternative conformations, as well as discretely separated alternative conformations that occupy distinct rotamers. Similar to the 2mFo-DFc electron density integration results for Phe113, we observed a large change in $\chi1$ bond order parameters at 240 K and above (**Figure 6 A**).

Mapping the Transitions in CypA Conformational Heterogeneity

Next, we applied the order parameter analysis to all sidechain $\chi1$ angles in CypA. Although conformational heterogeneity generally increases with temperature throughout the enzyme, we observed a diverse set of conformational responses (**Figure 6 – Figure S1**). The trends for the majority of residues suggested a transition somewhere between our data points at 180 and 240 K, below which the change in conformational heterogeneity with temperature is reduced. To quantify this trend, we performed separate fits for the low-temperature (≤180 K) and high-temperature (≥240 K) data points for all residues. The slopes of conformational heterogeneity ($1-S^2$) vs. temperature were significantly different ($p=1\times10^{-62}$, paired T-test) on either side of this transition range: the average slope for the low-temperature fit lines (2.5×10^{-4} K^{-1}) was an order of magnitude smaller than for the high-temperature fit lines (2.6×10^{-3} K^{-1}). This is consistent with the idea that heterogeneity is much less dependent on temperature below the 180-240 K "transition" range.

However, some residues behaved differently from the rest of the protein. Val2 retains its conformational heterogeneity at all temperatures, which is expected based on its weakly constrained position at the N-terminus. Many of the remaining outlier residues (Glu15, Glu81, Pro105, Ala117, Glu120, Lys125, Met142, Ser147, Lys151) appear to be involved in a spatially contiguous set of crystal contacts across symmetry mates in the

267 context of the crystal lattice (**Figure 6 - Figure S2**). This cluster includes Glu81, which adopts alternative
268 backbone conformations only at low temperatures (**Figure 4**). The variability of these residues can likely be
269 explained by distinct sets of conformations across crystal contacts that are differentially, but somewhat
270 stochastically, favored during the cooling process (Alcorn and Juers, 2010).
271
272 Our data suggest that CypA does not undergo a single global transition from having strongly temperature-
273 dependent changes in sidechain conformational heterogeneity to relatively temperature-independent behavior. An
274 "intersection" or "transition" temperature for each bond angle can be estimated from the intersection of the low-
275 temperature and high-temperature fit lines of $1\text{-}S^2$ versus temperature. The distribution of these intersection
276 temperatures is broad and asymmetrical, with an elongated tail from the peak near 250 K toward 200 K (**Figure 6**
277 **B**). Furthermore, the distribution of intersection temperatures is more complex for order parameters reporting on
278 the terminal heavy-atom bond of the sidechain than for $\chi1$ (**Figure 6 - Figure S3**, **Figure 6 - Figure S4**). This
279 increase likely occurs because sidechain end orientations are subject to more degrees of freedom and therefore
280 temperature changes may redistribute them in a greater variety of ways.
281
282 *Distinguishing Between Models of Protein Heterogeneity as a Function of Temperature*
283
284 Our data provide insight into models for the origin of the temperature dependence of protein conformational
285 heterogeneity and into proposed dynamical transitions. In one model, deactivation of different internal protein
286 motions at high temperatures (near 300 K) is sufficient to predict a dynamical transition near 200 K (Lee and
287 Wand, 2001). In a second model, solvent-coupled arrest of protein motions produces a transition in a similar
288 temperature range (Ringe and Petsko, 2003). To distinguish between these two models, we analyzed the average
289 sidechain disorder across all residues in CypA, focusing on the bond most closely associated with the $\chi1$ dihedral
290 angle, at each of the eight temperatures we studied (**Figure 6 C**). These averaged disorder values drop as
291 temperature is decreased from 310 K, then flatten out somewhere between 240 and 180 K, with some scatter due
292 to the variability in the cryocooling process (data points in **Figure 6 C**, **Figure 6 – Figure Supplement 7**).
293
294 Next, we used two different linear fits to extrapolate $1\text{-}S^2$ across all temperatures for each residue, floored the
295 result at maximum order ($1\text{-}S^2=0$), and then averaged across all residues to obtain predictions for the residue-
296 averaged disorder versus temperature. In the first fit, the linear function was fit to data for each residue at all
297 temperatures. Consistent with the necessity of using separate fit lines for the low-temperature and high-
298 temperature data (**Figure 5** and **Figure 6 – Figure S1**), the resulting prediction gives a poor account of the
299 averaged experimental data and does not indicate a transition (purple line in **Figure 6 C**). In the second fit, only
300 the high-temperature (240 K and above) data for each residue was fit. The resulting prediction is more consistent
301 with the averaged high-temperature experimental data, and does indicate a transition (red line in **Figure 6 C**). The
302 flattening of this predicted curve at low temperatures occurs as more individual residues achieve maximal

303 predicted order ($S^2 \rightarrow 1$) (**Figure 6 - Figure S5**). This latter prediction, which is extrapolated from high-
304 temperature crystallographic data, is reminiscent of predictions based on NMR relaxation experiments conducted
305 at 288-346 K (Lee and Wand, 2001). Our observations are consistent with the idea that thermal depopulation of
306 protein alternative conformations is sufficient to predict the existence of an average inflection without invoking a
307 transition of the solvent. However, the low temperature of the predicted inflection (~100 K), as well as the large
308 separation in low-temperature disorder between our experimental data (data points in **Figure 6 C**) and predictions
309 from high temperature (red line in **Figure 6 C**), suggest that thermal depopulation of protein alternative
310 conformations cannot by itself account for the observed ~200 K transition. This large separation also indicates
311 that data collected at high temperatures (>260 K) cannot be reliably extrapolated to predict conformational
312 heterogeneity at low temperatures. It also follows that data from low temperatures (≤180 K) cannot be simply
313 extrapolated to predict the features of the energy landscape that may be important above ~200 K.
314
315 Many effects may contribute to the discrepancy between the observed data and the behavior projected from the
316 high-temperature fits. To gain additional insight into this discrepancy, we decomposed the order parameters into
317 their B-factor vs. discrete-conformers components and examined their temperature dependences (**Figure 6 –**
318 **Figure S6**). Roughly 67% of residues (e.g., Phe8) remain within one rotamer well across all temperatures.
319 Approximately 13% of residues (e.g., Ser99 and Phe113) populate clearly separable multiple rotameric states at
320 high temperatures, and then show complete depopulation of minority states on cooling so that only a single
321 rotameric state remains at 180 K and below. However, 6% of residues (e.g., Thr5) continue to populate multiple
322 rotameric states at or below 180 K. An additional 6% of residues (e.g., Lys91) populate new rotameric states only
323 at or below 180 K. These results help explain the excess residual disorder in our experimental structures below
324 240 K compared to projections based on high-temperature fits. Although slopes of crystallographic B-factors with
325 temperature remain nearly flat below 240 K (**Figure 6 - Figure S2 B**), we expect that true harmonic thermal
326 disorder does subtly decrease from 180 to 100 K; these thermal effects could be more detectable if even higher-
327 resolution data were collected at even lower temperatures, perhaps by using liquid helium as a cryogen to cool to
328 ~15 K or below (Chinte et al., 2007).
329
330 *Imperfect Coupling Between Active-Site Residues in CypA*
331
332 While the results above show a variety of thermal and non-thermal conformational responses, it remains unclear
333 whether these responses involve coupled conformational shifts of multiple residues. In particular, the network of
334 alternative sidechain conformations spreading from the core of the protein (Ser99) into the active site (Arg55)
335 across multiple β-strands exhibits qualitatively similar behavior of increasing occupancy above 240 K. In previous
336 work (Fraser et al., 2009), the collective presence of these alternative conformations at room temperature, but not
337 at cryogenic temperatures, and the close contacts between these residues had suggested a concordance to the
338 single exchange process fit by NMR relaxation dispersion for this dynamic active-site network. However, using

339 our new multitemperature data, this network appears subdivided based on the apparent intersection or transition
340 temperatures of the constituent residues, with Ser99 and Phe113 behaving most similarly to each other (**Figure 7,**
341 **Movie 4**).
342
343 **Discussion**
344
345 Here we have mapped the conformational landscape of the dynamic enzyme CypA by analyzing multiconformer
346 models from multitemperature crystallography. Unlike previous temperature-dependent analyses of X-ray
347 crystallography, here we consider both harmonic disorder (B-factors) and non-harmonic displacements
348 (alternative conformations and occupancies), characterized using crystallographic bond order parameters. We
349 have four primary findings: (1) The occupancy of alternative sidechain conformations present at 310 K generally
350 decreases with decreasing temperature. (2) However, some residues adopt alternative conformations only at 180 K
351 and below. (3) The temperature response of residues is highly heterogeneous: the "intersection temperature"
352 below which sidechain conformational heterogeneity remains nearly constant has a broad distribution across the
353 molecule, with a peak near 250 K. (4) Residues composing a dynamic active-site network that is important for
354 function do not have a consistent intersection temperature.
355
356 Our results provide new insight into the relationship between energy landscapes, the glass transition, and protein
357 function. Glasses and other disordered systems have complex energy landscapes, in part due to the large number
358 of microenvironments and the extensive frustration that disorder generates in the intermolecular interactions.
359 Proteins at biological temperatures are "glassy" in this sense – they have complex energy landscapes, due to their
360 large size, heterogeneous amino acid composition, and many degrees of conformational freedom (Frauenfelder et
361 al., 1991). The extensive heterogeneity in the temperature response of individual residues in CypA we observe
362 here provides additional direct evidence for this underlying energetic heterogeneity.
363
364 In addition to the inherent "glassiness" of proteins at biological temperatures, dynamical transitions, some of
365 which have been called "glass transitions", have been reported at lower temperatures, including 180, 200, 220,
366 240, and 250 K, based on Mossbauer spectroscopy, X-ray crystallography, liquid and solid-state NMR, neutron
367 scattering, and other techniques (Lewandowski et al., 2015; Schiro et al., 2015). These transitions typically
368 manifest as a change in slope of some measurement in the vicinity of the suggested transition temperature.
369 However, many of these measurements are sensitive to motions only within some timescale window (often ps-ns),
370 monitor only a subset of amino acid types, and/or spatially average over all residues in the protein. By contrast,
371 multitemperature crystallography with multiconformer models has many advantages by providing a time-
372 independent and fully site-resolved measurement of ensemble-averaged atomic displacements, including both
373 harmonic and discrete conformational heterogeneity, within the crystal.
374

375 This combined methodology lets us examine dynamical and glass transitions in protein crystals from a new
376 perspective. Glass transitions are by definition non-equilibrium phenomena that arise when the kinetics of
377 relaxation toward equilibrium slow so dramatically that equilibrium cannot be reached on experimental
378 timescales. One signature of a true glass transition in proteins would be if occupancies of minority alternative
379 conformations were arrested at non-zero values below some temperature. Indeed, here we see no appreciable
380 temperature evolution of individual conformer occupancies or B-factors at 180 K and below, and the average
381 disorder at these temperatures is far in excess of what is predicted from high-temperature extrapolations. These
382 observations are consistent with the falling out of equilibrium expected in a glass transition, but not with a
383 transition driven by the thermal freeze-out of alternative sidechain conformations (Lee and Wand, 2001).
384 Moreover, the persistence of multiple rotameric states at low temperatures is consistent with solvent arrest that
385 impedes further changes in sidechain disorder. Although the details of protein-solvent interactions may differ in
386 crystals vs. in solution, local variability at different protein-solvent interface microenvironments in the crystal
387 (Teeter et al., 2001) likely contributes to the heterogeneity of temperature responses that we observe. The critical
388 importance of site resolution is evident in the results of Figure 6. Averaging over sidechain disorder in all
389 residues yields an apparent transition near 250 K (**Figure 6** and **Figure 6 - Figure S7**). Perhaps coincidentally,
390 this same temperature has been associated with a transition for protein sidechains in site-averaged solid-state
391 NMR measurements (Lewandowski et al., 2015). However, the "transition" in our residue-averaged result
392 obscures the highly heterogeneous temperature dependence of the individual sidechains. We find no evidence of
393 tight cooperativity or of a collective global response near 250 K that would be expected in the case of a "true"
394 dynamical transition Instead, our data are consistent with local, non-cooperative freeze-out of conformational
395 states defined by the energy landscape over a broad temperature range.
396
397 The heterogeneous response of sidechain order parameters to temperature is driven largely by the changes to the
398 populations of alternative conformations, which "flat-line" at different temperatures across CypA. This diversity
399 of "flat-lining" temperatures is present even within the dynamic active-site network, even though the constituent
400 residues have similar occupancies for their major and minor states at high temperatures (**Figure 7**). This result
401 contrasts with previous NMR and X-ray experiments that hypothesized correlated motions of this network as rate-
402 limiting for the catalytic cycle (Eisenmesser et al., 2005; Fraser et al., 2009) (**Figure 8 A**). To bridge these views,
403 we propose that the active-site network adopts two substates, which are primarily distinguished by Phe113
404 rotamer interconversion. Each of these substates adopts a differently weighted ensemble of conformations for
405 other residues (**Figure 8 B**). In this model, Met61 and Arg55 can switch rotamers more easily than Ser99 when
406 Phe113 is in its $\chi1$ gauche+ (p) rotamer pointed toward Ser99, whereas Ser99 can switch rotamers more easily
407 than Met61 and Arg55 when Phe113 is in its $\chi1$ gauche- (m) rotamer pointed toward Met61. Additionally, thermal
408 "breathing" motions within rotameric wells may relieve minor steric overlaps within some of these macro- and
409 microstates (**Figure 8 B**, bottom right). This model is consistent with Phe113 having the lowest "flat-lining"
410 temperature of the network (**Figure 7**), and makes sense sterically because of the large size of the aromatic ring.

411 These hypothesized motions are consistent with the timescales and temperature dependencies of motion assigned
412 by solid-state NMR studies of crystalline protein GB1 (Lewandowski et al., 2015). Furthermore, the model helps
413 explain the difficulty of fitting NMR relaxation data for perturbed versions of the active-site network as a single
414 collective exchange process (Schlegel et al., 2009). The aromatic ring of Phe113 could play a dominant role in
415 determining the chemical shift changes of the surrounding residues. Each of these residues could also populate
416 multiple rotamers in the excited state measured by NMR. Our hierarchical perspective evokes the "population
417 shuffling" model of (Smith et al., 2015), in which a protein macrostate (in CypA, defined by the Phe113 rotamer)
418 also determines the different relative populations of rotamers for a subset of other residues (in CypA, the other
419 residues in the active-site network). In this model, the interconversion between macrostates, and not the collective
420 motion of all residues between distinct rotamers, is correlated with the rate-limiting step of the CypA catalytic
421 cycle.
422
423 Diversity in the temperature dependences of alternative conformations as we see here is inevitable given the
424 limitations of the amino acid alphabet, yet its spatial pattern within a protein may provide insight into selective
425 pressures. Evolutionary optimization must ensure that functionally important alternative conformations are
426 robustly populated and interconvert appreciably at physiological conditions. However, the energy landscapes of
427 individual residues are coupled to varying extents, such that some subsets of residues must be collectively
428 optimized to preserve some, but not perfect, collectivity in functional motions. For proteins with large sequence
429 alignments, evolutionary covariation has been used to predict "sectors" of functionally cooperative residues,
430 which are often dispersed in primary sequence but strikingly contiguous in tertiary structure (Halabi et al., 2009).
431 By contrast, temperature-dependent crystallography has the potential to unveil couplings in atomic detail by
432 identifying sets of residues whose conformational ensembles respond concertedly to temperature change. Based
433 on our results with CypA, we expect this coupling to be weak, but measurable. Serial femtosecond XFEL
434 crystallography combined with ultra-fast temperature jumps could enable a temporal view of these coupled
435 conformational changes. Novel static and time-resolved multitemperature crystallographic approaches will
436 provide powerful tools for resolving concerted motions to explore how proteins function and evolve.

437 **Methods**
438
439 *Protein expression, purification, and crystallization.*
440 Wildtype CypA was produced and crystallized as previously reported (Fraser et al., 2009). Briefly, crystals were
441 grown by mixing equal volumes of well solution (100 mM HEPES pH 7.5, 23% PEG 3350, 5 mM TCEP) and
442 protein (60 mg mL^{-1} in 20 mM HEPES pH 7.5, 100 mM NaCl, 0.5 mM TCEP) in the hanging-drop format.
443
444 *Crystallographic data collection.*
445 For the multitemperature synchrotron datasets at 100, 150, 180, 240, 260, 280, 300, and 310 K, we collected data
446 at the Cornell High Energy Synchrotron Source (CHESS) at beamline A1 with a 100 micron collimator using a
447 wavelength of 0.9767 Å. Crystals were looped by hand, stripped of excess mother liquor (100 mM HEPES pH
448 7.5, 23% PEG 3350, 5 mM TCEP) using NVH oil (Warkentin and Thorne, 2009), and placed directly into the
449 nitrogen-gas cryostream pre-set to the desired temperature at the beamline. Water inside protein crystals is
450 nanoconfined so that ice nucleation is dramatically suppressed, but water outside crystallizes readily and rapidly.
451 Careful removal of all excess solvent from the crystal surface is essential to obtaining ice-free diffraction between
452 260 K and 180 K without using large cryoprotectant concentrations .
453
454 For the XFEL experiment, we collected multiple diffraction images per crystal using a 10 micron X-ray beam
455 with each irradiation point separated by at least 25-40 microns to avoid collateral radiation damage. A total of
456 1,239 still diffraction images were collected from 71 CypA crystals over the course of two experiments using a
457 goniometer setup and a Rayonix MX325HE detector at LCLS-XPP (Cohen et al., 2014) (**Movie 1**). All data was
458 collected at ambient temperature (approximately 273 K). To prevent dehydration, crystals were coated with
459 paratone oil immediately after looping and mounted on the goniometer at the XPP end station of LCLS using the
460 SAM sample exchange robot (Cohen et al., 2002).
461
462 For the new 1.2 Å room-temperature synchrotron dataset, paratone oil was applied to cover a 2 µL hanging drop
463 containing a single large crystal of CypA. The crystal was harvested through the paratone and excess mother
464 liquor was removed using a fine paper wick. Attenuated data was collected at SSRL beamline 11-1 at 273 K
465 controlled by the cryojet on the PILATUS 6M PAD detector.
466
467 *Crystallographic data processing.*
468 The synchrotron datasets were indexed, integrated, and scaled using XDS and XSCALE, and intensities were
469 subsequently converted to structure factor amplitudes using XDSCONV. All datasets were from single crystals.
470 Data reduction statistics for the highest-resolution room-temperature dataset and the multitemperature datasets can
471 be found in **Table 4** and **Table 1,** respectively.
472
473 The XFEL data were processed using *cctbx.xfel* (Hattne et al., 2014). Of the 1,239 images collected, 772 were
474 indexed and their intensities were integrated. Post-refinement, as implemented by *PRIME* (**p**ost-**r**ef**i**nement and
475 **me**rging, version date: Nov 11 20:22:51 2014)(Uervirojnangkoorn et al., 2015), was used to correct the intensity
476 measurements and merge the data. We optimized over the uc_tolerance, n-postref_cycle, sigma_min,
477 partiality_min, and gamma_e values to obtain the final structure factor amplitudes. Data reduction statistics for
478 the XFEL data are provided in **Table 3**.
479
480 To promote consistency between models derived from different data sets, R_{free} flags were generated using
481 *PHENIX* for the highest-resolution "reference" (1.2 Å 273 K) dataset first, and were subsequently copied to all
482 other multitemperature and XFEL datasets for the automated molecular replacement and refinement pipeline.
483

Model building.

For each dataset, we calculated initial phases by performing molecular replacement with *phenix.auto_mr* using PDB ID 2cpl as a search model. We next refined XYZs and ADPs of the initial model with *phenix.refine* for 4 macrocycles with XYZ and ADP weight optimization turned on; identified TLS groups with *phenix.find_tls_groups*; and refined optimized XYZs, ADPs, and TLS parameters for 6 more macrocycles. These single-conformer models and associated electron density maps were used as input for two subsequent steps.

First, the single-conformer models were analyzed with Ringer (Lang et al., 2010) via *mmtbx.ringer* using default settings. A coupled sidechain-backbone "backrub" motion (Davis et al., 2006) of -10˚ for Ser99 (see **Figure 5A**) was necessary to match the Cα and Cβ positions of the minor conformation as modeled in PDB ID 3K0N; using this modified backbone indeed yielded maximal minor-conformation Ringer peaks for our multitemperature datasets. No backrub motion was necessary for Leu98 due to the different type of backbone displacement (Fraser et al., 2009). Correlation coefficients between pairs of Ringer electron density vs. dihedral angle curves were calculated using the *cor* function in R (Team, 2014).

Second, the single-conformer models were used as input to *qFit* (Keedy et al., 2014; van den Bedem et al., 2009). Subsequent to the automated model building, we manually deleted ill-fitting waters and edited alternative protein sidechain conformations based on fit to the electron density in *Coot* (Emsley et al., 2010) and refinement with *phenix.refine*. For example, at 240 K, *qFit* automatically modeled Phe113 as single-state, but significant +mFo-DFc peaks remained, so we decided on a two-state model. Met61 was particularly difficult to model accurately across temperatures due to convolved issues of $\chi3$ non-rotamericity for Met in general (Butterfoss et al., 2005), the relatively high electron count for sulfur, and likely temperature-modulated Met-specific radiation damage. For these reasons, visual inspection of the maps and manual building is currently essential for alternative backbone conformations with moderate displacements, as observed in residues 79-83 (**Figure 4**). We are currently developing new methods to automatically detect and model such backbone excursions in multiscale multiconformer models. These efforts improved R_{free} and MolProbity scores across datasets (**Table 2**). Because of the lower resolution, the XFEL model was refined with three TLS groups and with optimization of X-ray vs. geometry and ADP weights.

Model and electron density analysis.

For minor-state electron density sums, 2mFo-DFc (Fc filled) map values were summed across a grid of points defined by superimposing each model onto PDB ID 3k0n using all Cα atoms, summing the 2mFo-DFc value at each point with 0.25 Å of a target minor-state heavy atom (Oγ for Ser99; Cδ1, Cε1, Cε2, or Cζ for Phe113), and normalizing to unity across datasets for each residue being analyzed. This procedure allowed a strictly common reference set of map evaluation points. Results were very similar when using unfilled maps (data not shown).

We calculated B-factor-influenced order parameters (S^2) as previously reported (Fenwick et al., 2014) except that we monitored one of two different types of bond vector. For the $\chi1$ order parameter, we used Cβ-Xβ (where X = C or O) for most amino acids, Cα-Cβ for Ala, and Cα-Hα for Gly. For the sidechain-end order parameter, we used the heavy-atom to heavy-atom bond vector for each amino acid that was closest to the sidechain terminus, with ties broken by the number in the atom name (e.g. Cγ-Cδ1 instead of Cγ-Cδ2 for Leu). All negative order parameters (caused by high B-factors) were floored to 0. $\chi1$ order parameters were floored for 7 residues, and sidechain-end order parameters were floored for 23 residues. Per-residue "apparent dynamic transition temperatures" were then calculated as the intersection between the <200 K and >200 K fit lines in order parameter vs. temperature plots and floored to 0 K if necessary. The kernel density curve was fit with the *density* function in R (Team, 2014).

For extrapolation of fit lines in **Figure 6**, we used a fit to all data points or to just the high-temperature data points (≥240 K) for each residue, and extrapolated to the temperature at which order would be maximized ($1 - S^2 = 0$). To predict global behavior, at each temperature we averaged across all residues the predicted $1 - S^2$ values from the fit, making sure to floor non-physical predicted values of $1 - S^2 < 0$ to 0, as in (Lee and Wand, 2001).

Acknowledgements

We thank Justin Biel, Bryn Fenwick, Robert Stroud, Ian Wilson, and Peter Wright for helpful conversations.
D.A.K. is supported by an A.P. Giannini Postdoctoral Research Fellowship.
R.A.W. is supported by a NSF Graduate Research Fellowship.
M.C.T. is supported by a BioXFEL Postdoctoral Fellowship.
N.K.S. and A.S.B. are supported by NIH GM095887 and NIH GM102520
A.T.B. and W.I.W. acknowledge a Howard Hughes Medical Institute Collaborative Innovation Award (HCIA) that also provided funds for the purchase of the microdiffractometer for the goniometer setup.
H.v.d.B. is supported by the NIH Protein Structure Initiative U54GM094586 at the Joint Center for Structural Genomics and SLAC National Accelerator Laboratory grant SLAC-LDRD-0014-13-2.
R.E.T. is supported by NSF MCB-1330685.
J.S.F. is a Searle Scholar, Pew Scholar, and Packard Fellow, and is supported by NIH OD009180, NIH GM110580, and NSF STC-1231306.
Use of the Linac Coherent Light Source (LCLS), SLAC National Accelerator Laboratory, is supported by the U.S. Department of Energy, Office of Science, Office of Basic Energy Sciences under Contract No. DE-AC02-76SF00515.
Use of the Cornell High Energy Synchrotron Source (CHESS) is supported by NSF DMR-1332208. The Macromolecular Diffraction at CHESS (MacCHESS) facility is supported by NIH GM103485.
Use of the Stanford Synchrotron Radiation Lightsource, SLAC National Accelerator Laboratory, is supported by the U.S. Department of Energy, Office of Science, Office of Basic Energy Sciences under Contract No. DE-AC02-76SF00515. The SSRL Structural Molecular Biology Program is supported by the DOE Office of Biological and Environmental Research, and NIH GM103393.

The authors declare that no competing interests exist.

References

Alcorn, T., and Juers, D.H. (2010). Progress in rational methods of cryoprotection in macromolecular crystallography. Acta crystallographica Section D, Biological crystallography *66*, 366-373.

Baldwin, A.J., and Kay, L.E. (2009). NMR spectroscopy brings invisible protein states into focus. Nature chemical biology *5*, 808-814.

Burnley, B.T., Afonine, P.V., Adams, P.D., and Gros, P. (2012). Modelling dynamics in protein crystal structures by ensemble refinement. eLife *1*, e00311.

Butterfoss, G.L., Richardson, J.S., and Hermans, J. (2005). Protein imperfections: separating intrinsic from extrinsic variation of torsion angles. Acta crystallographica Section D, Biological crystallography *61*, 88-98.

Chinte, U., Shah, B., Chen, Y.S., Pinkerton, A.A., Schall, C.A., and Hanson, B.L. (2007). Cryogenic (<20 K) helium cooling mitigates radiation damage to protein crystals. Acta crystallographica Section D, Biological crystallography *63*, 486-492.

Cohen, A.E., Ellis, P.J., Miller, M.D., Deacon, A.M., and Phizackerley, R.P. (2002). An automated system to mount cryo-cooled protein crystals on a synchrotron beam line, using compact sample cassettes and a small-scale robot. Journal of applied crystallography *35*, 720-726.

Cohen, A.E., Soltis, S.M., Gonzalez, A., Aguila, L., Alonso-Mori, R., Barnes, C.O., Baxter, E.L., Brehmer, W., Brewster, A.S., Brunger, A.T., *et al.* (2014). Goniometer-based femtosecond crystallography with X-ray free electron lasers. Proceedings of the National Academy of Sciences of the United States of America *111*, 17122-17127.

Davis, I.W., Arendall, W.B., 3rd, Richardson, D.C., and Richardson, J.S. (2006). The backrub motion: how protein backbone shrugs when a sidechain dances. Structure *14*, 265-274.

Deis, L.N., Pemble, C.W.t., Qi, Y., Hagarman, A., Richardson, D.C., Richardson, J.S., and Oas, T.G. (2014). Multiscale conformational heterogeneity in staphylococcal protein a: possible determinant of functional plasticity. Structure *22*, 1467-1477.

Doster, W. (2010). The protein-solvent glass transition. Biochim Biophys Acta *1804*, 3-14.

Doster, W., Cusack, S., and Petry, W. (1989). Dynamical transition of myoglobin revealed by inelastic neutron scattering. Nature *337*, 754-756.

Dror, R.O., Dirks, R.M., Grossman, J.P., Xu, H., and Shaw, D.E. (2012). Biomolecular simulation: a computational microscope for molecular biology. Annual review of biophysics *41*, 429-452.

Eisenmesser, E.Z., Bosco, D.A., Akke, M., and Kern, D. (2002). Enzyme dynamics during catalysis. Science *295*, 1520-1523.

Eisenmesser, E.Z., Millet, O., Labeikovsky, W., Korzhnev, D.M., Wolf-Watz, M., Bosco, D.A., Skalicky, J.J., Kay, L.E., and Kern, D. (2005). Intrinsic dynamics of an enzyme underlies catalysis. Nature *438*, 117-121.

Emsley, P., Lohkamp, B., Scott, W.G., and Cowtan, K. (2010). Features and development of Coot. Acta crystallographica Section D, Biological crystallography *66*, 486-501.

Fenwick, R.B., van den Bedem, H., Fraser, J.S., and Wright, P.E. (2014). Integrated description of protein dynamics from room-temperature X-ray crystallography and NMR. Proceedings of the National Academy of Sciences of the United States of America *111*, E445-454.

Fraser, J.S., Clarkson, M.W., Degnan, S.C., Erion, R., Kern, D., and Alber, T. (2009). Hidden alternative structures of proline isomerase essential for catalysis. Nature *462*, 669-673.

Fraser, J.S., van den Bedem, H., Samelson, A.J., Lang, P.T., Holton, J.M., Echols, N., and Alber, T. (2011). Accessing protein conformational ensembles using room-temperature X-ray crystallography. Proceedings of the National Academy of Sciences of the United States of America *108*, 16247-16252.

Frauenfelder, H., Chen, G., Berendzen, J., Fenimore, P.W., Jansson, H., McMahon, B.H., Stroe, I.R., Swenson, J., and Young, R.D. (2009). A unified model of protein dynamics. Proceedings of the National Academy of Sciences of the United States of America *106*, 5129-5134.

Frauenfelder, H., Hartmann, H., Karplus, M., Kuntz, I.D., Jr., Kuriyan, J., Parak, F., Petsko, G.A., Ringe, D., Tilton, R.F., Jr., Connolly, M.L., *et al.* (1987). Thermal expansion of a protein. Biochemistry *26*, 254-261.

Frauenfelder, H., Petsko, G.A., and Tsernoglou, D. (1979). Temperature-dependent X-ray diffraction as a probe of protein structural dynamics. Nature *280*, 558-563.

611 Frauenfelder, H., Sligar, S.G., and Wolynes, P.G. (1991). The energy landscapes and motions of proteins. Science
612 *254*, 1598-1603.

613 Fukuda, Y., and Inoue, T. (2015). High-temperature and high-resolution crystallography of thermostable copper
614 nitrite reductase. Chemical communications.

615 Garman, E.F. (2010). Radiation damage in macromolecular crystallography: what is it and why should we care?
616 Acta crystallographica Section D, Biological crystallography *66*, 339-351.

617 Halabi, N., Rivoire, O., Leibler, S., and Ranganathan, R. (2009). Protein sectors: evolutionary units of three-
618 dimensional structure. Cell *138*, 774-786.

619 Halle, B. (2004). Biomolecular cryocrystallography: structural changes during flash-cooling. Proceedings of the
620 National Academy of Sciences of the United States of America *101*, 4793-4798.

621 Hattne, J., Echols, N., Tran, R., Kern, J., Gildea, R.J., Brewster, A.S., Alonso-Mori, R., Glockner, C., Hellmich,
622 J., Laksmono, H.*, et al.* (2014). Accurate macromolecular structures using minimal measurements from X-ray
623 free-electron lasers. Nature methods *11*, 545-548.

624 Henzler-Wildman, K., and Kern, D. (2007). Dynamic personalities of proteins. Nature *450*, 964-972.

625 Hirata, K., Shinzawa-Itoh, K., Yano, N., Takemura, S., Kato, K., Hatanaka, M., Muramoto, K., Kawahara, T.,
626 Tsukihara, T., Yamashita, E.*, et al.* (2014). Determination of damage-free crystal structure of an X-ray-sensitive
627 protein using an XFEL. Nature methods *11*, 734-736.

628 Holton, J.M. (2009). A beginner's guide to radiation damage. Journal of synchrotron radiation *16*, 133-142.

629 Keedy, D.A., van den Bedem, H., Sivak, D.A., Petsko, G.A., Ringe, D., Wilson, M.A., and Fraser, J.S. (2014).
630 Crystal cryocooling distorts conformational heterogeneity in a model michaelis complex of DHFR. Structure *22*,
631 899-910.

632 Kern, J., Tran, R., Alonso-Mori, R., Koroidov, S., Echols, N., Hattne, J., Ibrahim, M., Gul, S., Laksmono, H.,
633 Sierra, R.G.*, et al.* (2014). Taking snapshots of photosynthetic water oxidation using femtosecond X-ray
634 diffraction and spectroscopy. Nature communications *5*, 4371.

635 Lang, P.T., Holton, J.M., Fraser, J.S., and Alber, T. (2014). Protein structural ensembles are revealed by
636 redefining X-ray electron density noise. Proceedings of the National Academy of Sciences of the United States of
637 America *111*, 237-242.

638 Lang, P.T., Ng, H.L., Fraser, J.S., Corn, J.E., Echols, N., Sales, M., Holton, J.M., and Alber, T. (2010).
639 Automated electron-density sampling reveals widespread conformational polymorphism in proteins. Protein
640 science : a publication of the Protein Society *19*, 1420-1431.

641 Lee, A.L., and Wand, A.J. (2001). Microscopic origins of entropy, heat capacity and the glass transition in
642 proteins. Nature *411*, 501-504.

643 Lewandowski, J.R., Halse, M.E., Blackledge, M., and Emsley, L. (2015). Protein dynamics. Direct observation of
644 hierarchical protein dynamics. Science *348*, 578-581.

645 Motlagh, H.N., Wrabl, J.O., Li, J., and Hilser, V.J. (2014). The ensemble nature of allostery. Nature *508*, 331-339.

646 Ollikainen, N., Smith, C.A., Fraser, J.S., and Kortemme, T. (2013). Flexible backbone sampling methods to
647 model and design protein alternative conformations. Methods in enzymology *523*, 61-85.

648 Rejto, P.A., and Freer, S.T. (1996). Protein conformational substates from X-ray crystallography. Progress in
649 biophysics and molecular biology *66*, 167-196.

650 Ringe, D., and Petsko, G.A. (2003). The 'glass transition' in protein dynamics: what it is, why it occurs, and how
651 to exploit it. Biophysical chemistry *105*, 667-680.

652 Schiro, G., Fichou, Y., Gallat, F.X., Wood, K., Gabel, F., Moulin, M., Hartlein, M., Heyden, M., Colletier, J.P.,
653 Orecchini, A.*, et al.* (2015). Translational diffusion of hydration water correlates with functional motions in
654 folded and intrinsically disordered proteins. Nature communications *6*, 6490.

655 Schlegel, J., Armstrong, G.S., Redzic, J.S., Zhang, F., and Eisenmesser, E.Z. (2009). Characterizing and
656 controlling the inherent dynamics of cyclophilin-A. Protein science : a publication of the Protein Society *18*, 811-
657 824.

658 Schlichting, I. (2015). Structural biology: Photosynthetic complex in close-up. Nature *517*, 26-27.

659 Smith, C.A., Ban, D., Pratihar, S., Giller, K., Schwiegk, C., de Groot, B.L., Becker, S., Griesinger, C., and Lee, D.
660 (2015). Population shuffling of protein conformations. Angew Chem Int Ed Engl *54*, 207-210.

661 Smith, J.L., Hendrickson, W.A., Honzatko, R.B., and Sheriff, S. (1986). Structural heterogeneity in protein
662 crystals. Biochemistry *25*, 5018-5027.

663 Spence, J.C., Weierstall, U., and Chapman, H.N. (2012). X-ray lasers for structural and dynamic biology. Reports
664 on progress in physics Physical Society *75*, 102601.

665 Suga, M., Akita, F., Hirata, K., Ueno, G., Murakami, H., Nakajima, Y., Shimizu, T., Yamashita, K., Yamamoto,
666 M., Ago, H.*, et al.* (2015). Native structure of photosystem II at 1.95 A resolution viewed by femtosecond X-ray
667 pulses. Nature *517*, 99-103.

668 Team, R. (2014). R: A Language and Environment for Statistical Computing (Vienna, Austria: R Foundation for
669 Statistical Computing).

670 Teeter, M.M., Yamano, A., Stec, B., and Mohanty, U. (2001). On the nature of a glassy state of matter in a
671 hydrated protein: Relation to protein function. Proceedings of the National Academy of Sciences of the United
672 States of America *98*, 11242-11247.

673 Tilton, R.F., Jr., Dewan, J.C., and Petsko, G.A. (1992). Effects of temperature on protein structure and dynamics:
674 X-ray crystallographic studies of the protein ribonuclease-A at nine different temperatures from 98 to 320 K.
675 Biochemistry *31*, 2469-2481.

676 Uervirojnangkoorn, M., Zeldin, O.B., Lyubimov, A.Y., Hattne, J., Brewster, A.S., Sauter, N.K., Weis, W.I., and
677 Brunger, A.T. (2015). Enabling X-ray Free Electron Laser Crystallography for Challenging Biological Systems
678 from a Limited Number of Crystals. eLife *In Press*.

679 van den Bedem, H., Bhabha, G., Yang, K., Wright, P.E., and Fraser, J.S. (2013). Automated identification of
680 functional dynamic contact networks from X-ray crystallography. Nature methods *10*, 896-902.

681 van den Bedem, H., Dhanik, A., Latombe, J.C., and Deacon, A.M. (2009). Modeling discrete heterogeneity in X-
682 ray diffraction data by fitting multi-conformers. Acta crystallographica Section D, Biological crystallography *65*,
683 1107-1117.

684 van den Bedem, H., and Fraser, J.S. (2015). Integrative, Dynamic Structural Biology at Atomic Resolution—It's
685 About Time. Nature methods *In Press*.

686 Warkentin, M., Badeau, R., Hopkins, J.B., and Thorne, R.E. (2012). Spatial distribution of radiation damage to
687 crystalline proteins at 25-300 K. Acta crystallographica Section D, Biological crystallography *68*, 1108-1117.

688 Warkentin, M., Hopkins, J.B., Badeau, R., Mulichak, A.M., Keefe, L.J., and Thorne, R.E. (2013). Global
689 radiation damage: temperature dependence, time dependence and how to outrun it. Journal of synchrotron
690 radiation *20*, 7-13.

691 Warkentin, M., and Thorne, R.E. (2009). Slow cooling of protein crystals. Journal of applied crystallography *42*,
692 944-952.

693 Woldeyes, R.A., Sivak, D.A., and Fraser, J.S. (2014). E pluribus unum, no more: from one crystal, many
694 conformations. Current opinion in structural biology *28*, 56-62.
695

	100 K	150 K	180 K	240 K	260 K	280 K	300 K	310 K
PDB ID	4YUG	4YUH	4YUI	4YUJ	4YUK	4YUL	4YUM	4YUN
Wavelength	0.9767	0.9767	0.9767	0.9767	0.9767	0.9767	0.9767	0.9767
Resolution range	33.58 - 1.48 (1.53 - 1.48)	16.95 - 1.34 (1.39 - 1.34)	16.12 - 1.38 (1.43 - 1.38)	34.05 - 1.42 (1.47 - 1.42)	33.98 - 1.48 (1.53 - 1.48)	25.23 - 1.42 (1.47 - 1.42)	22.67 - 1.5 (1.55 - 1.50)	22.66 - 1.58 (1.64 - 1.58)
Space group	$P2_12_12_1$	$P2_12_12_1$	$P2_12_12_1$	$P2_12_12_1$	$P2_12_12_1$	$P2_12_12_1$	$P2_12_12_1$	$P2_12_12_1$
Unit cell (a, b, c)	42.24 51.91 88.06	42.45 51.82 88.01	42.42 51.96 88.21	43.04 53.22 88.63	43.09 52.79 88.81	43.00 52.61 89.12	43.01 52.61 89.32	42.85 52.58 89.41
Total reflections	160129 (15842)	160780 (7437)	154202 (11295)	152578 (13600)	134699 (13381)	168932 (15019)	144734 (14433)	125225 (12326)
Unique reflections	32657 (3240)	42288 (3471)	39548 (3820)	38881 (3710)	34411 (3391)	38763 (3794)	32999 (3254)	28291 (2760)
Multiplicity	4.9 (4.9)	3.8 (2.1)	3.9 (3.0)	3.9 (3.7)	3.9 (3.9)	4.4 (4.0)	4.4 (4.4)	4.4 (4.5)
Completeness (%)	99 (100)	95 (80)	97 (95)	99 (96)	100 (100)	100 (100)	99 (100)	100 (100)
Mean I/sigma(I)	14.07 (1.57)	25.95 (3.24)	16.47 (1.64)	12.86 (1.66)	10.09 (1.46)	15.51 (1.52)	16.90 (1.63)	13.26 (1.45)
Wilson B-factor	16.07	13.12	16.95	15.55	16.06	17.62	19.75	21.44
R-merge (%)	6.8 (99.4)	3.0 (29.4)	4.2 (71.8)	6.2 (99.2)	8.1 (104.3)	4.9 (100.0)	4.7 (101.7)	6.7 (127.3)
R-meas (%)	7.6 (111.0)	3.4 (36.9)	4.8 (85.6)	7.2 (116.8)	9.4 (120.8)	5.6 (115.3)	5.4 (115.9)	7.6 (144.5)
CC1/2	1.00 (0.62)	1.00 (0.90)	1.00 (0.60)	1.00 (0.50)	1.00 (0.52)	1.00 (0.52)	1.00 (0.59)	1.00 (0.56)
CC*	1.00 (0.88)	1.00 (0.97)	1.00 (0.87)	1.00 (0.82)	1.00 (0.83)	1.00 (0.83)	1.00 (0.86)	1.00 (0.85)
Refinement resolution range	33.085 - 1.48 (1.558 - 1.48)	19.117 - 1.34 (1.394 - 1.34)	16.995 - 1.38 (1.435 - 1.38)	34.055 - 1.42 (1.477 - 1.42)	33.98 - 1.48 (1.547 - 1.48)	25.23 - 1.42 (1.477 - 1.42)	22.67 - 1.5 (1.579 - 1.5)	25.222 - 1.58 (1.679 - 1.58)
Reflections used in refinement	32627 (4654)	42278 (3932)	39545 (4265)	38879 (4161)	34411 (4237)	38762 (4256)	32999 (4643)	28287 (4632)
Reflections used for R-free	1028 (147)	1325 (125)	1238 (133)	1218 (130)	1080 (133)	1217 (133)	1036 (145)	889 (146)

R-work (%)	13.3 (20.4)	12.4 (16.4)	13.3 (25.4)	12.6 (26.3)	13.1 (26.0)	11.1 (22.6)	10.8 (20.0)	11.7 (21.8)
R-free (%)	18.3 (26.8)	15.6 (21.3)	17.5 (33.0)	15.6 (30.4)	16.8 (31.2)	14.3 (25.5)	14.4 (24.8)	15.0 (28.8)
Number of non-hydrogen atoms	2279	2433	1969	1993	2035	2120	2096	2172
Macromolecule atoms	1933	2132	1745	1750	1837	1924	1952	2061
Protein residues	165	164	164	163	163	163	163	163
RMS(bonds)	0.009	0.008	0.008	0.009	0.009	0.008	0.009	0.009
RMS(angles)	1.16	1.20	1.23	1.20	1.16	1.16	1.14	1.14
Ramachandran favored (%)	97	94	97	96	97	96	97	96
Ramachandran allowed (%)	3.3	5.7	2.7	4.1	3	4.2	3.3	3.9
Ramachandran outliers (%)	0	0	0	0	0	0	0	0
Rotamer outliers (%)	2.4	1.3	0.53	1.1	1.5	1.9	1.4	0.88
Clashscore	0.57	1.08	0.00	1.24	0.27	0.78	0.52	0.00
Average B-factor	21.74	17.25	21.85	20.14	20.00	21.48	24.09	25.77
Macromolecule Average B-factor	18.48	14.67	19.99	17.95	18.17	19.61	22.82	24.94
Solvent Average B-factor	39.99	35.54	36.34	35.89	37.01	39.89	41.23	41.30

Table 1: Crystallographic statistics for multitemperature synchrotron datasets collected on a single crystal per dataset. Statistics for the highest-resolution shell are shown in parentheses.

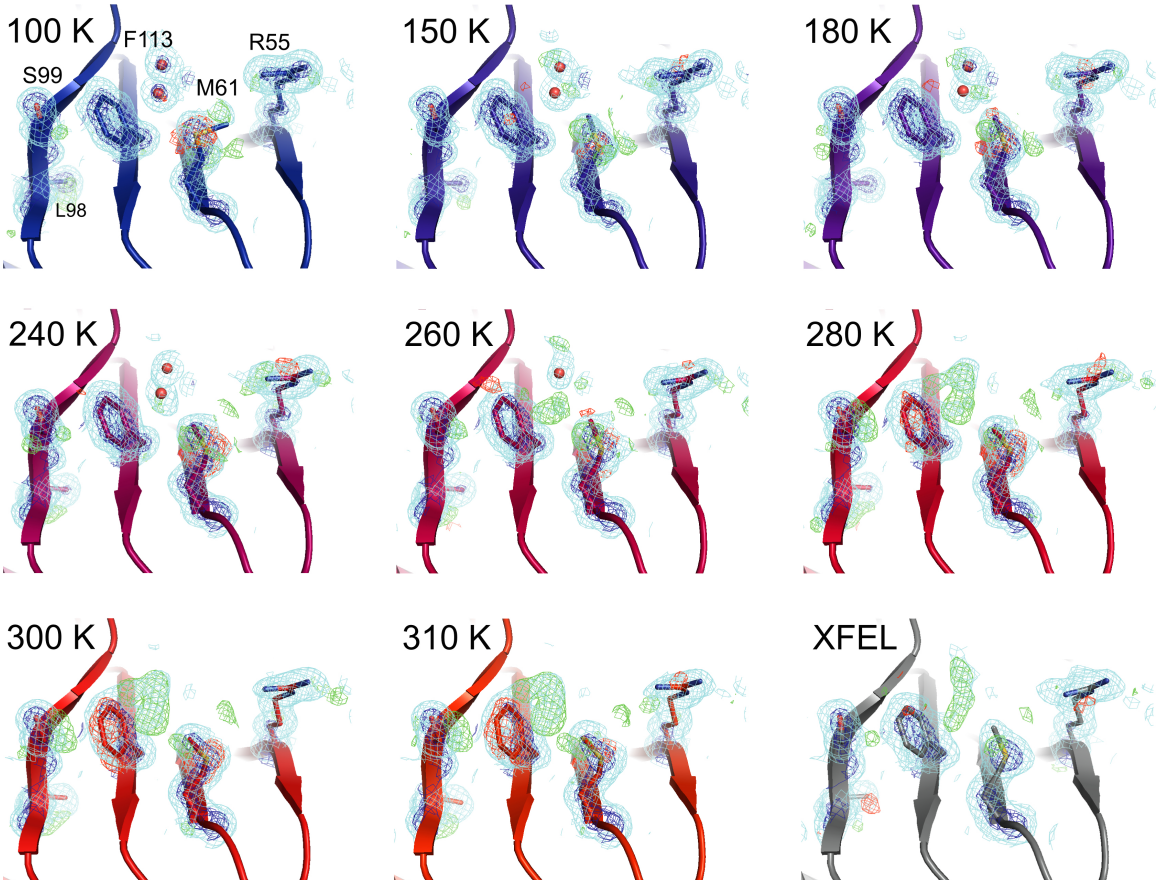

Table 1 - Figure Supplement 1: Single-conformer models cannot explain the crystallographic data at higher temperatures. The CypA dynamic network is shown after molecular replacement and refinement (including automated water placement) in PHENIX, before any manual rebuilding. The major state is well supported by 2mFo-DFc electron density contoured at 0.6 σ (cyan mesh) and 3.0 σ (dark blue mesh) for all datasets, but mFo-DFc difference electron density becomes more negative for the major state (-3.0 σ, red mesh) and more positive for the unmodeled minor state (+3.0 σ, green mesh) as temperature increases across the synchrotron datasets (blue to red), especially at and above 240 K. Full-occupancy water molecules (red spheres) are automatically placed by PHENIX near the Phe113 minor state in lower-temperature, but not in higher-temperature synchrotron models because they are mutually exclusive with the secondary Phe113 conformation.

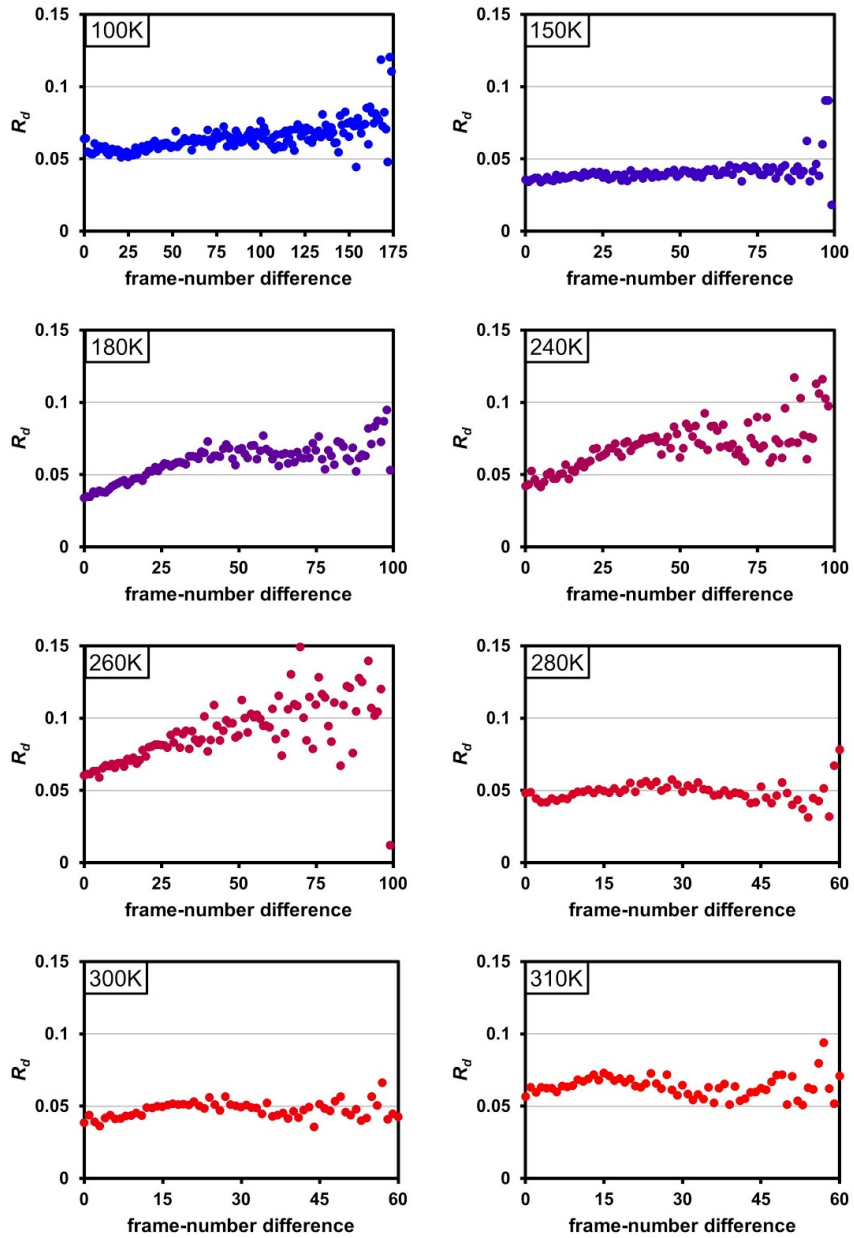

Table 1 - Figure Supplement 2: Radiation damage is minimal across data collection temperatures. Plots of R_d vs. frame-number difference for each dataset in the multitemperature trajectory reveal only minimal radiation damage. The datasets around 180-260 K exhibit higher R_d in later frames, which may reflect either a time-dependent cryocooling artifact or radiation damage at these intermediate temperatures. Although the rate of X-ray damage varies strongly with temperature, the data collection strategy was adjusted to yield a comparable amount of damage per frame. Therefore, there is no correlation between data collection temperature and the overall extent of radiation damage; the highest temperature data sets are equally undamaged as the lowest temperature data sets. By contrast, we observe a strong correlation between data collection temperature and conformational heterogeneity.

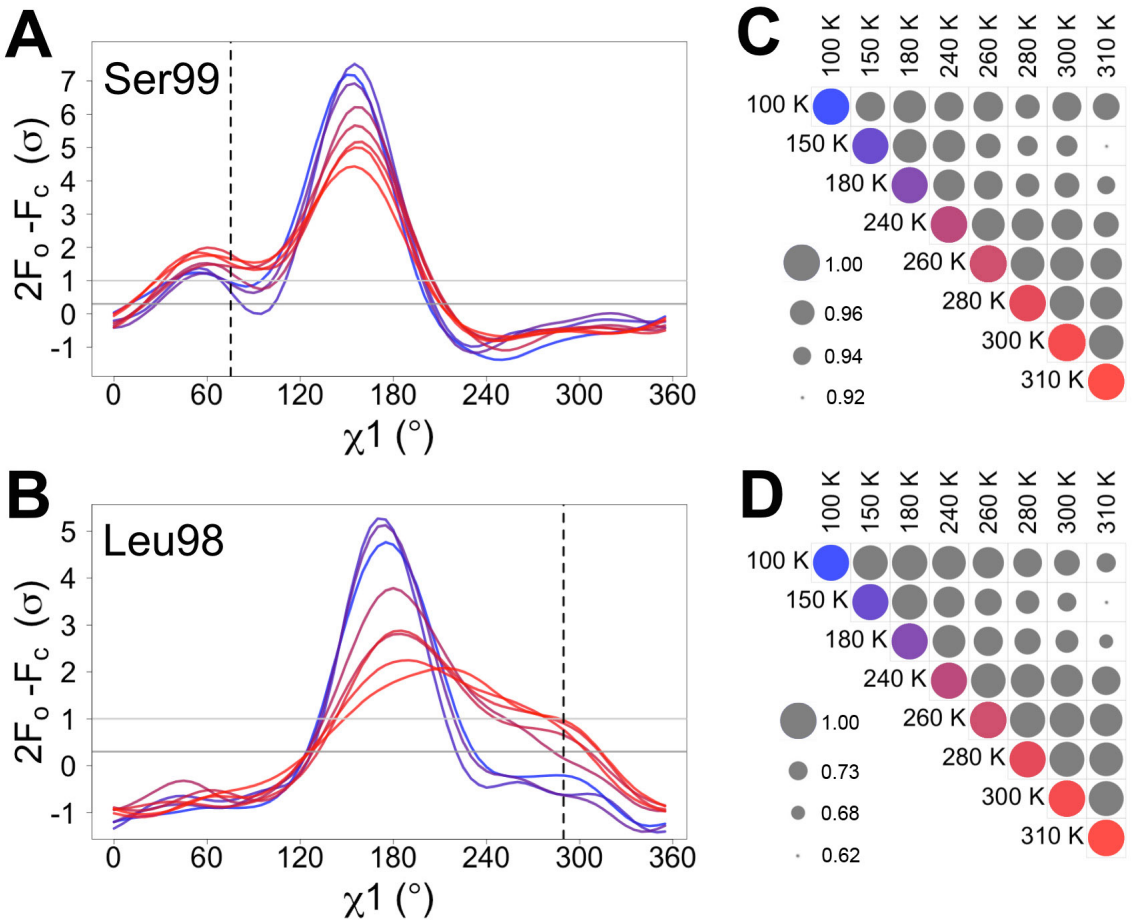

Figure 1: Automated electron density sampling reveals increased conformational redistribution. Ringer curves of 2mFo-DFc electron density vs. χ1 dihedral angle for **(A)** Ser99 and **(B)** Leu98 show large peaks for modeled major conformations, and also smaller peaks for additional minor conformations (dashed vertical lines). These secondary peaks become more evident as temperature increases (color gradient from blue to purple to red). A backrub motion was used for Ser99. For **(C)** Ser99 and **(D)** Leu98, a Pearson correlation coefficient was calculated between each pair of Ringer curves from the corresponding panel in **(A)** and **(B)**. Circles in diagonal elements are colored as in (**A)** and **(B)**; circles in off-diagonal elements are all gray but scaled by pairwise correlation coefficient (see legend). Pairs of curves from similar temperatures are generally more correlated to each other (larger circles) than are pairs of curves from more different temperatures (smaller circles).

		RT sync	XFEL	100 K	150 K	180 K	240 K	260 K	280 K	300 K	310 K
R_{free} (%)	*raw qFit*	16.7	25.2	19.0	16.9	18.5	17.5	17.9	15.7	16.3	16.1
	final	14.6	24.9	18.3	15.6	17.5	15.6	16.8	14.3	14.4	15.0
	Δ	-2.1	-0.3	-0.7	-1.3	-1.0	-1.9	-1.1	-1.4	-1.9	-1.1
Molprobity score	*raw qFit*	1.47	1.80	1.79	1.31	1.21	1.18	1.45	1.28	0.95	1.19
	final	1.08	1.39	1.19	1.29	0.63	1.14	0.91	1.25	0.99	0.76
	Δ	-0.39	-0.41	-0.80	-0.02	-0.58	-0.04	-0.54	-0.03	+0.04	-0.43

Table 2: Improvements in validation statistics from finalizing raw qFit models. Statistics calculated with *phenix.molprobity*.

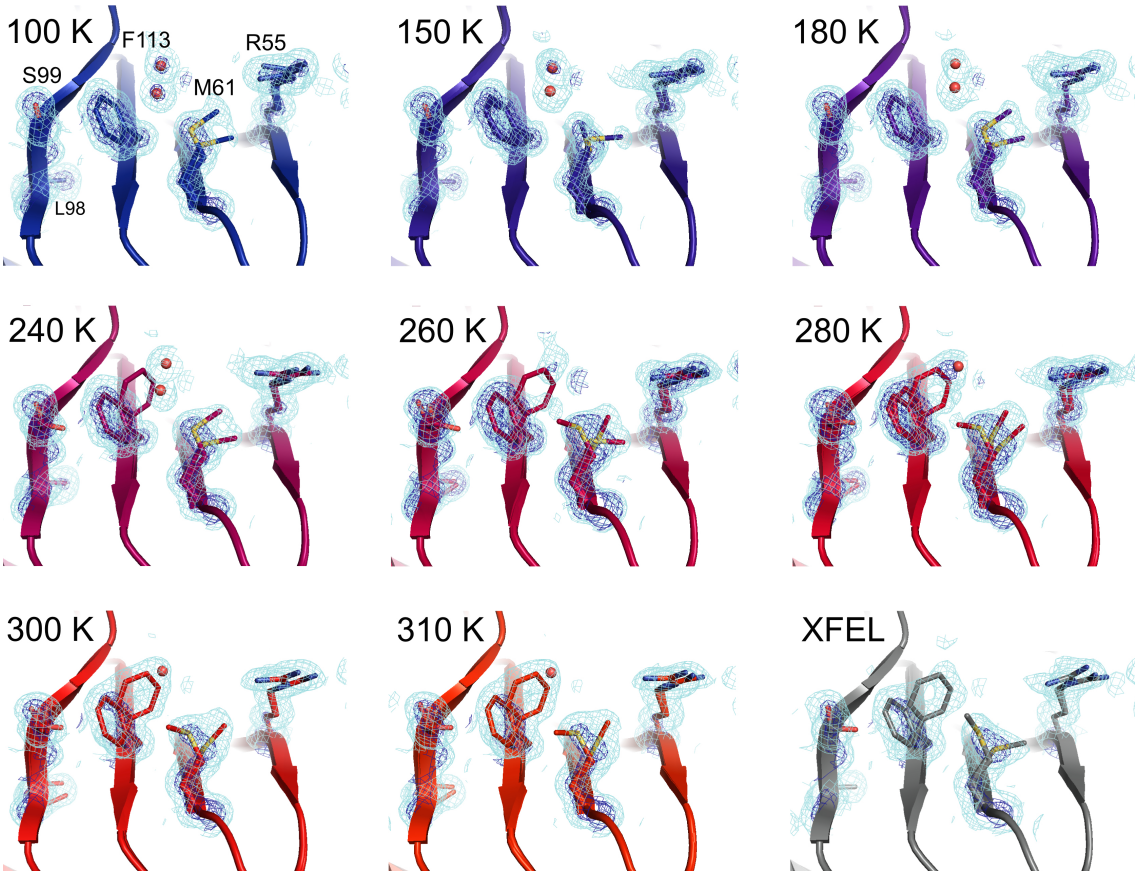

Figure 2: Multiconformer modeling across temperatures captures increasing conformational heterogeneity. Residues extending from the core to the active site of CypA adopt a single conformer at low temperatures, but gradually transition to increasing occupancy of secondary conformations as temperature increases. These conformations are well supported by 2mFo-DFc electron density contoured at 0.6 σ (cyan mesh) and 3.0 σ (dark blue mesh). This is corroborated by the room-temperature XFEL model (gray), which is free from conventional radiation damage and features the same secondary conformations. Water molecules (red spheres) are more fully ordered at low temperatures, but become only partially occupied at higher temperatures because they are mutually exclusive with the secondary Phe113 conformation.

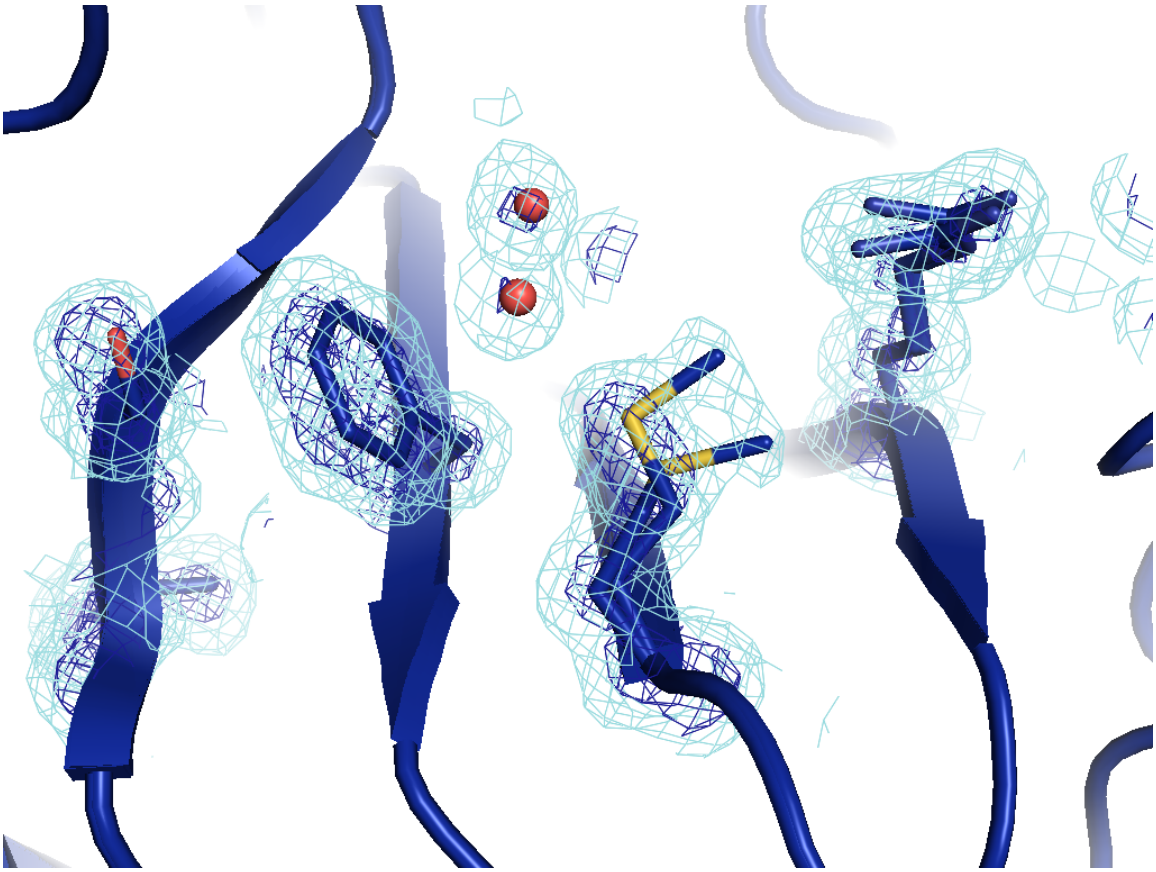

Movie 1: Animated interpolation between electron density maps in temperature trajectory. For each pair of adjacent temperatures (e.g. 100 and 150 K), the temperature regime between them was bisected and an average 2mFo-DFc electron density maps was calculated in reciprocal space using CCP4 utilities, until temperature points were spaced by <1 K. A new multiconformer model is shown when the animation reaches the corresponding temperature.

	XFEL
PDB ID	4YUP
Resolution range	43.98 - 1.75 (1.81 - 1.75)
Space group	$P2_12_12_1$
Unit cell (a, b, c)	42.42 51.82 87.96
Unique reflections	19942 (1894)
Completeness (%)	99 (96)
Wilson B-factor	21.12
Refinement resolution range	43.98 - 1.75 (1.93 - 1.75)
Reflections used in refinement	19936 (4811)
Reflections used for R-free	625 (151)
R-work (%)	20.0 (34.3)
R-free (%)	24.9 (36.1)
Number of non-hydrogen atoms	1762
Macromolecular atomcs	1559
Protein residues	164
RMS(bonds)	0.017
RMS(angles)	1.44
Ramachandran favored (%)	96
Ramachandran allowed (%)	3.6
Ramachandran outliers (%)	0
Rotamer outliers (%)	1.8
Clashscore	1.92
Average B-factor	29.03
macromolecules	26.52
solvent	48.25
Number of TLS groups	3

Table 3: Crystallographic statistics for room-temperature XFEL dataset collected across 71 crystals. Statistics for the highest-resolution shell are shown in parentheses.

	1.2 Å synchrotron
PDB ID	4YUO
Wavelength	0.9795
Resolution range	44.60 - 1.20 (1.24 - 1.20)
Space group	P 21 21 21
Unit cell	42.9 52.43 89.11 90 90 90
Total reflections	307722 (18999)
Unique reflections	58118 (5122)
Multiplicity	5.3 (3.7)
Completeness (%)	91 (82)
Mean I/sigma(I)	10.99 (5.93)
Wilson B-factor	15.22
R-merge (%)	11.2 (20.4)
R-meas (%)	12.2 (23.4)
CC1/2	0.99 (0.96)
CC*	1.00 (0.99)
Refinement resolution range	45.19 - 1.20 (1.23 - 1.20)
Reflections used in refinement	58108 (3657)
Reflections used for R-free	2000 (126)
R-work (%)	12.7 (31.3)
R-free (%)	14.6 (33.5)
Number of non-hydrogen atoms	2327
Macromolecular atoms	2143
Protein residues	163
RMS(bonds)	0.009
RMS(angles)	1.16
Ramachandran favored (%)	96
Ramachandran allowed (%)	4.1
Ramachandran outliers (%)	0
Rotamer outliers (%)	0.84
Clashscore	0.98
Average B-factor	19.62
macromolecules	18.40
solvent	33.86

Table 4: Crystallographic statistics for room-temperature synchrotron dataset collected on a single crystal. Statistics for the highest-resolution shell are shown in parentheses.

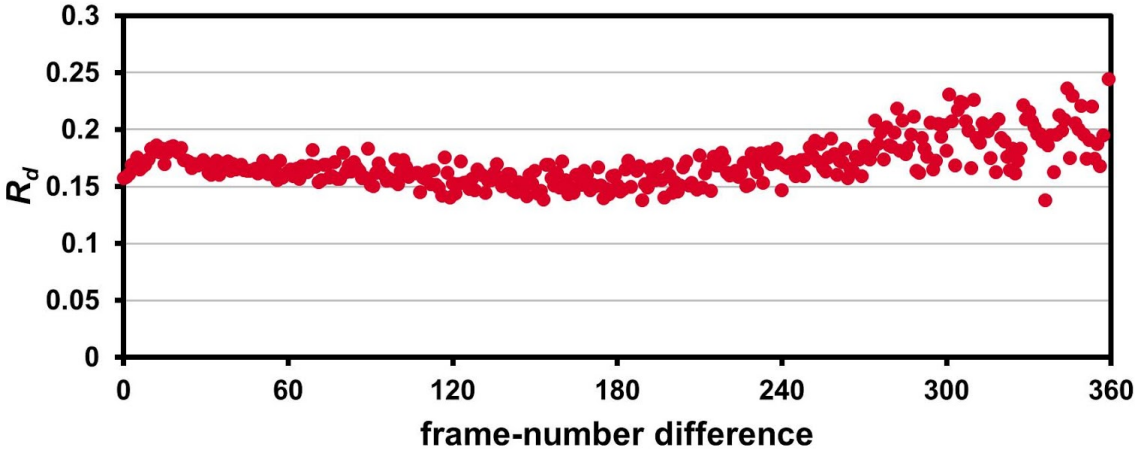

Table 4 - Figure Supplement 1: The 1.2 Å room-temperature CypA synchrotron data shows no signs of radiation damage. A plot of "decay *R*-factor" (R_d) as a function of frame-number difference (as in **Table 1 - Figure Supplement 2**) has a slope of zero, indicating the absence of radiation damage. R_d is calculated using pairwise observations of unique reflections (*hkl*) with centroids on frames *i* and *j*, and the frame-number difference is given by |*i*-*j*|. The calculations were performed using a 2.0 Å resolution cutoff.

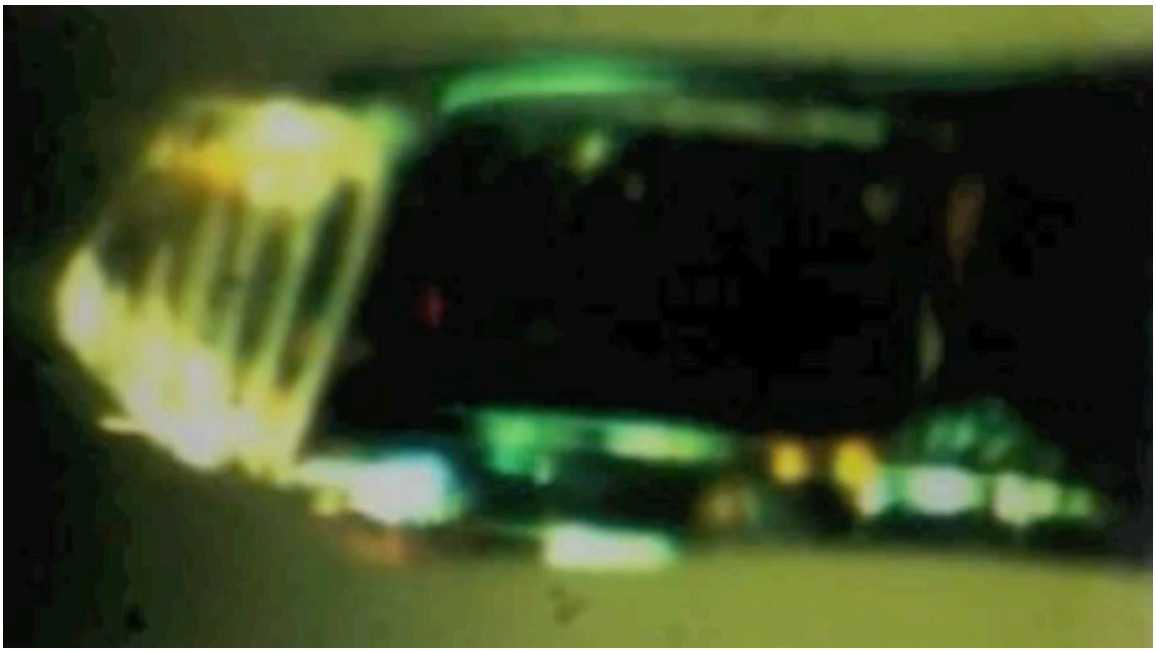

Movie 2: Fixed-target XFEL data collection from CypA crystals at the LCLS XPP end station. Screen capture image of the Blu-Ice GUI showing a video display of a CypA crystal. After each shot, a new damage line appears and the crystal is translated.

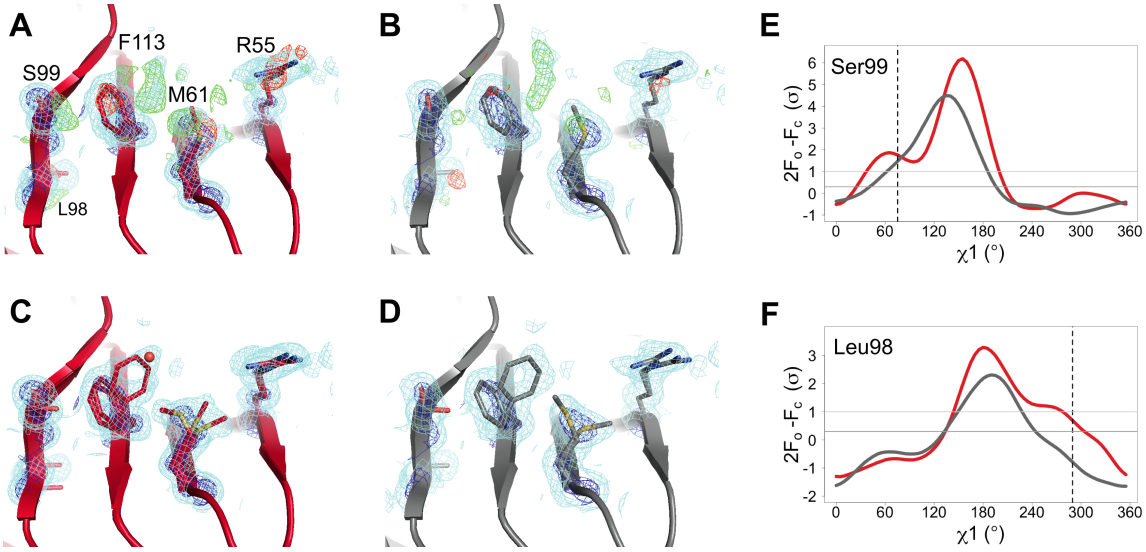

Figure 3: The active-site conformational ensemble of CypA determined without radiation damage at room temperature. (A) Electron density maps for room-temperature synchrotron (red) and (**B**) XFEL (silver) single-conformer models reveal conformational heterogeneity extending from the protein core (Leu98 and Ser99) to the active site (Arg55) of CypA. The primary conformation is well supported by 2mFo-DFc electron density contoured at 0.6 σ (cyan mesh) and 3.0 σ (dark blue mesh). mFo-DFc difference electron density contoured at 3.0 σ (green mesh) and -3.0 σ (red mesh) suggests unmodeled alternative conformations. **(C,D)** Finalized multiconformer models explicitly model these alternative conformations, which are well-supported by 2mFo-DFc electron density. **(E,F)** Ringer electron-density sampling for the single-conformer models shows peaks representing alternative conformations for **(E)** Ser99 and **(F)** Leu98. The primary conformations of both residues are obvious as peaks for both models, but the minor conformations (dashed vertical line; as modeled in 3k0n) are also evident, with 2mFo-DFc values well above the 0.3 σ (darker gray horizontal line) threshold, except for the Leu98 in the XFEL model (due to the lower resolution). A backrub motion of -10˚ positions the backbone properly for Ringer to best detect the minor conformation for Ser99, but not for Leu98.

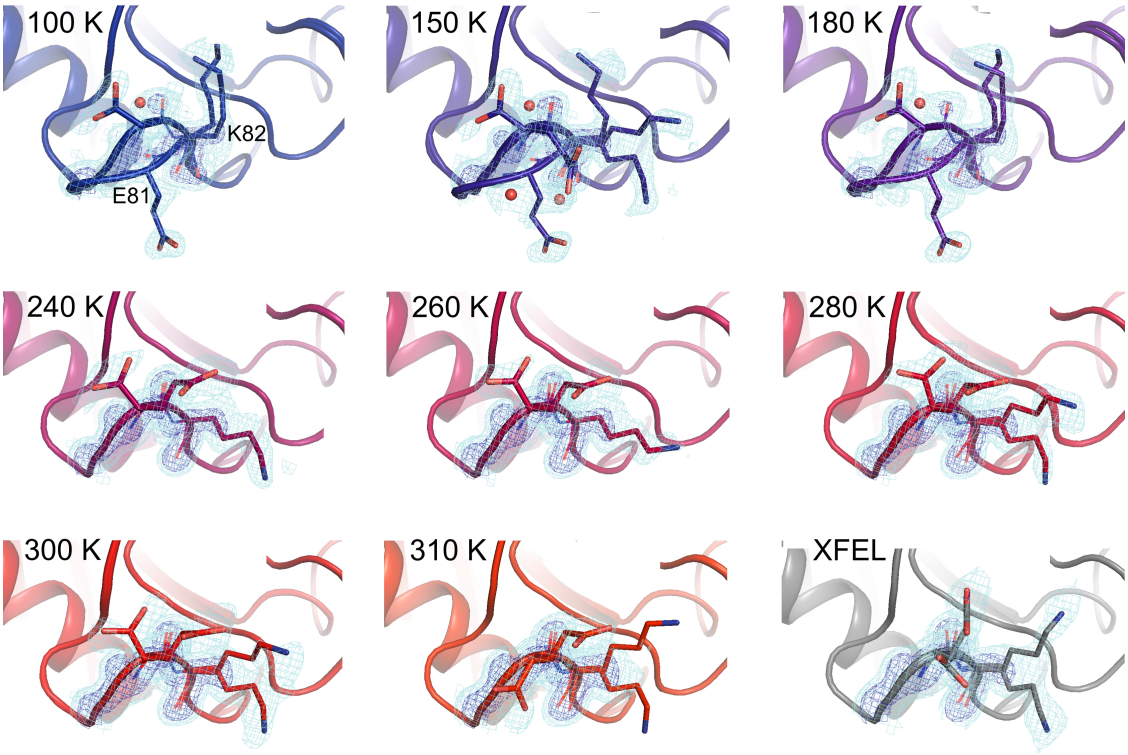

Figure 4: Alternative loop conformations can appear at lower temperatures. The surface loop containing residues 79-83 adopts alternative conformations at low temperatures (top row) but not at high temperatures (bottom two rows). The secondary loop conformation is separated from the body of the protein by an ordered water molecule (red sphere); the van der Waals interactions between the loop and the water may reflect an enthalpic stabilization that is more dominant at low temperatures. The electron density peak to the right of the water corresponds to the backbone carbonyl oxygen of Glu81. 2mFo-DFc electron density contoured at 0.6 σ (cyan mesh) and 2.0 σ (dark blue mesh).

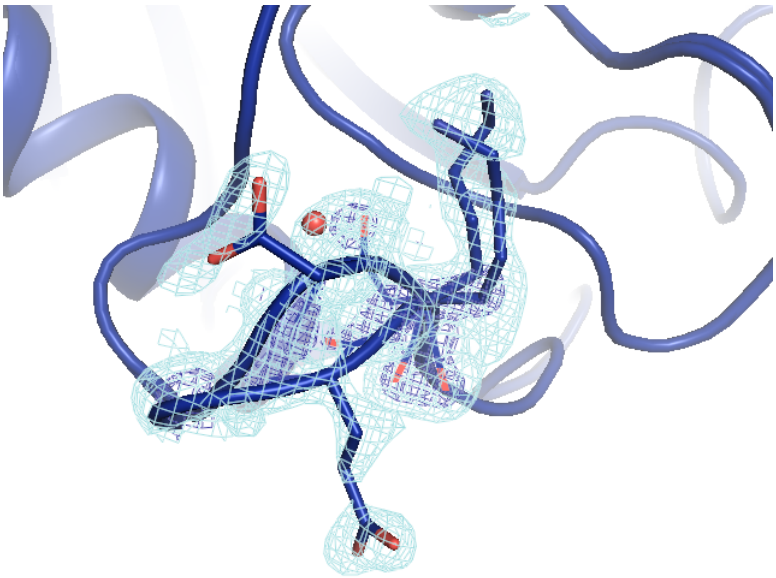

Movie 3: Animated rotation around the 100 K (blue) and 310 K (red) models and electron density maps from **Figure 4**.

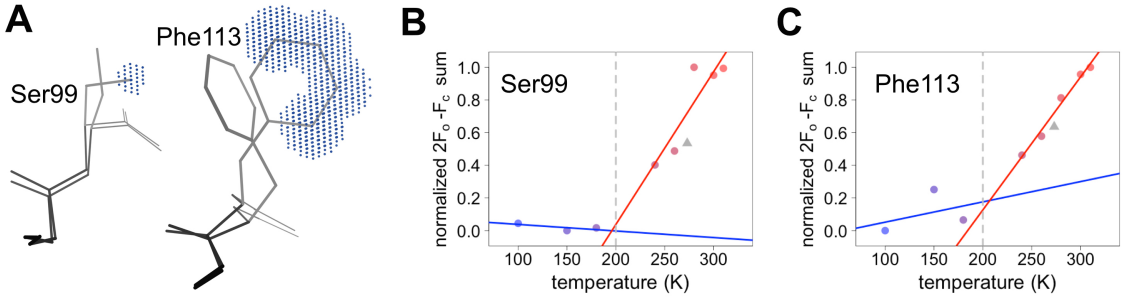

Figure 5: Quantifying temperature titration of conformational heterogeneity in multiconformer models. (A) 2mFo-DFc electron density was summed over the volume occupied by the minor conformation but not the major conformation (blue grid points) for Ser99 and Phe113. **(B,C)** Minor-state 2mFo-DFc electron density increases with temperature. Electron density sums were normalized for each residue. Multitemperature points from synchrotron data are shown in colors corresponding to temperature. The XFEL point is shown as a gray triangle. Best-fit lines are shown for 180 K and below (blue) vs. 240 K and above (red).

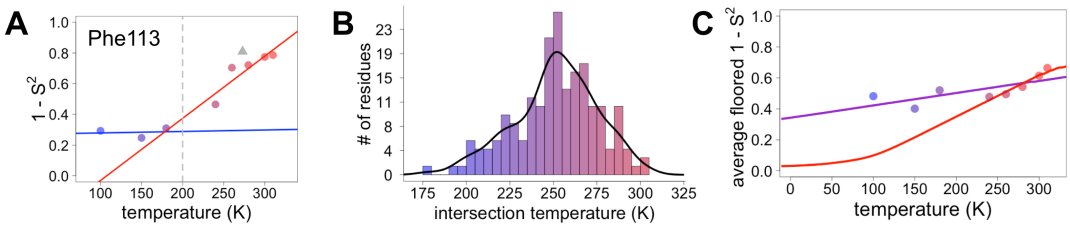

Figure 6: Diversity in temperature dependences of sidechain disorder across CypA does not predict the observed average arrest of disorder. (A) The complement of B-factor-influenced sidechain order parameter for the bond most closely associated with the χ1 dihedral angle for Phe113. Lines reflect least-squares fits to synchrotron models at 180 K and below (blue) vs. 240 K and above (red). Multitemperature synchrotron points in colors; XFEL point (not included in fits) as gray triangle. **(B)** Distribution of the intersection temperature between the <200 and >200 K lines fitted with kernel density function. The peak is near 250 K, although there is a tail toward lower temperatures. Intersection temperatures were <170 K for 4 residues and >330 K for 5 residues. **(C)** Predicted and observed values for the complement of sidechain order parameter, averaged over all residues in CypA. The predicted values were obtained by extrapolating each residue's fit line for 240 K and above (red curve) or for the full 100-300 K (purple curve), flooring the result to 0, then averaging across all residues in CypA. Observed values, similarly floored and averaged, are shown as points.

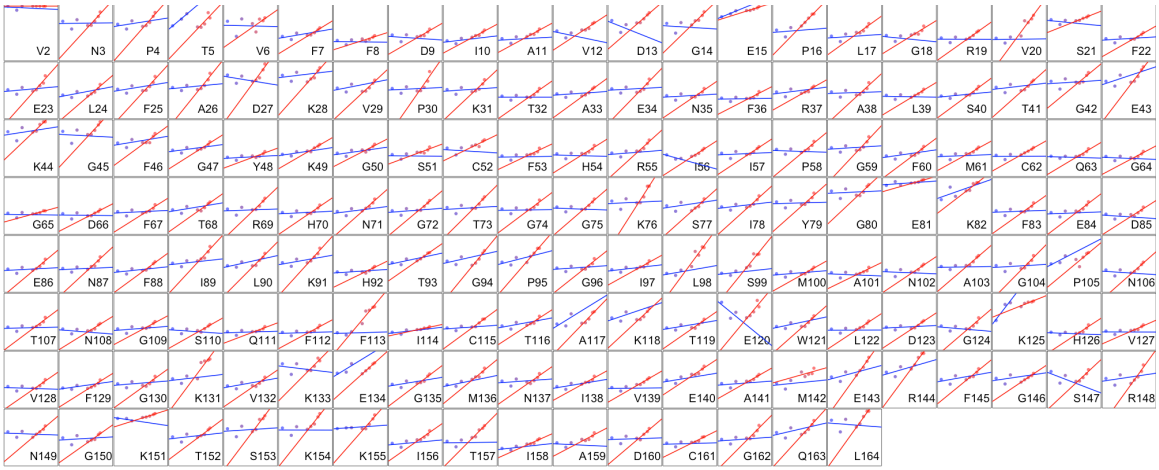

Figure 6 - Figure Supplement 1: Heterogeneous response of sidechain disorder to temperature. The complement of B-factor-influenced sidechain order parameter for the bond most closely associated with the χ1 dihedral angle for all residues in CypA. Lines reflect least-squares fits to synchrotron models for 180 K and below (blue) vs. 240 K and above (red).

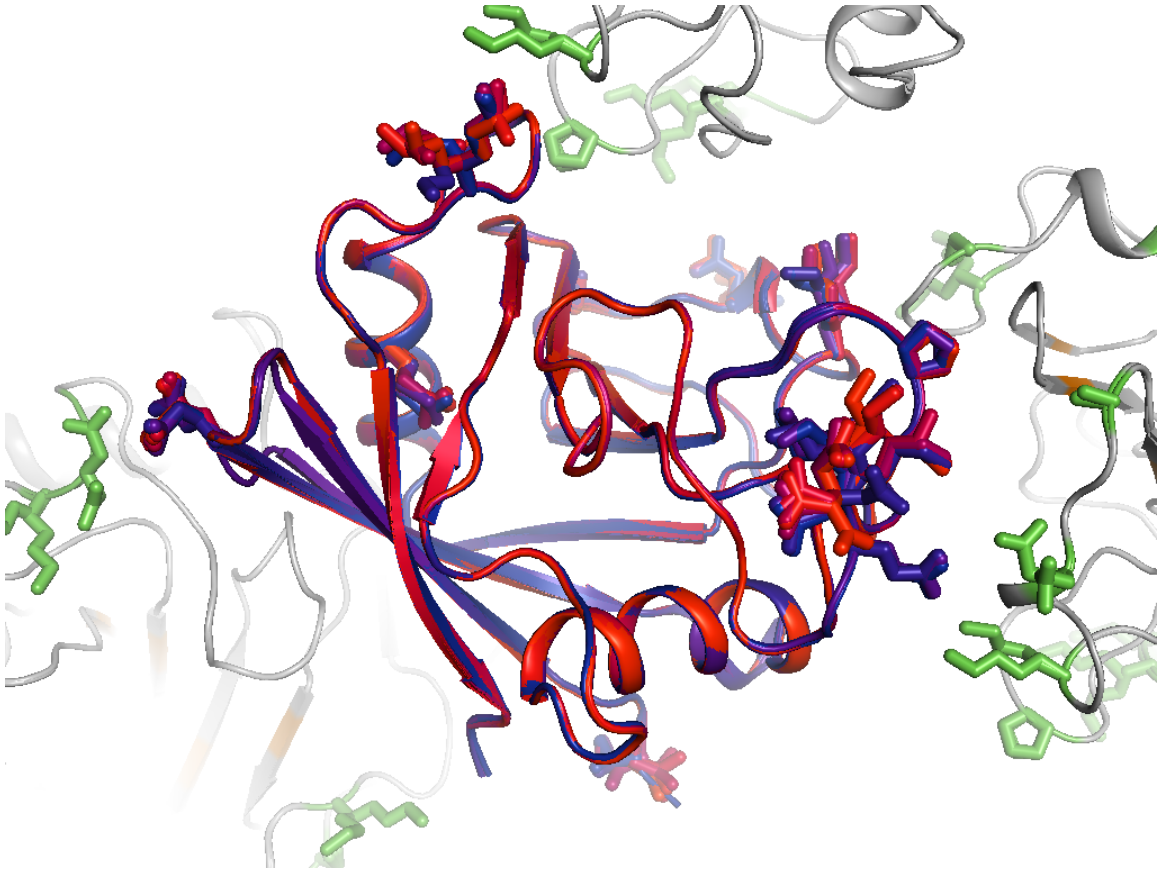

Figure 6 - Figure Supplement 2: Residues with persistent disorder across temperatures are inter-connected in the crystal lattice. Several residues with high 1 - S^2 values (Val2, Glu15, Gly80, Glu81, Lys82, Pro105, Ala117, Glu120, Lys125, Met142, Ser147, and Lys151) are shown for the central molecule (blue-to-red sticks and backbone) and also in symmetry mates (green sticks, gray backbone). Many of these residues appear to interact with each other via lattice contacts. Frustration in these interactions may lead to persistent disorder.

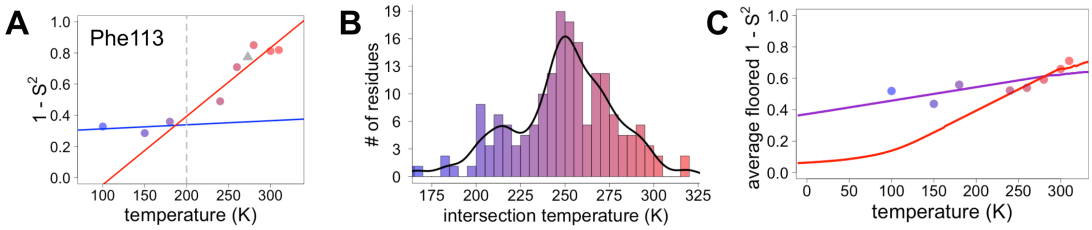

Figure 6 - Figure Supplement 3: Diversity in temperature dependences of sidechain-end disorder across CypA does not predict the observed average arrest of disorder. Each panel is as in **Figure 6**, but the order parameter now models the final heavy-atom to heavy-atom bond for each sidechain (see Methods).

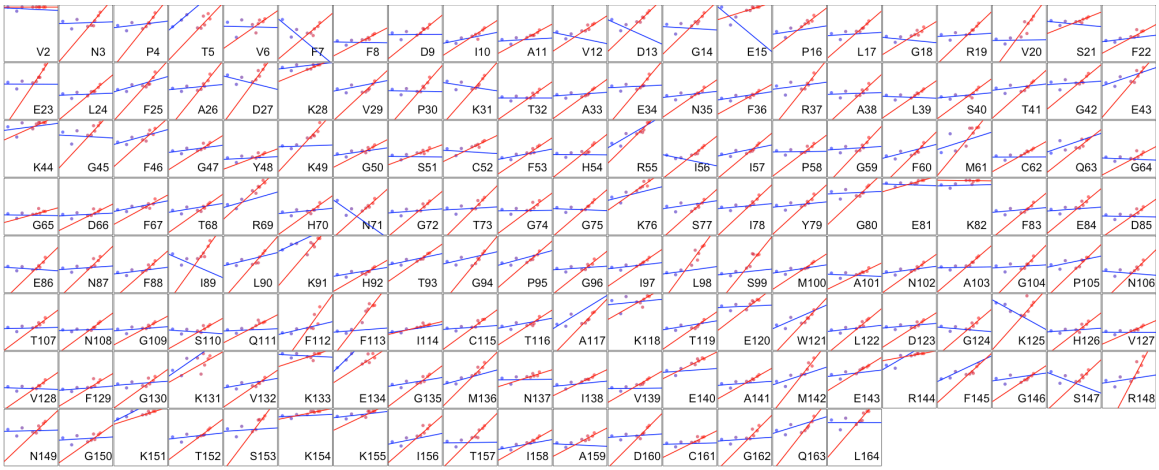

Figure 6 - Figure Supplement 4: Heterogeneous response of sidechain-end disorder to temperature. The small multiple plots are as in **Figure 6 - Figure Supplement 1**, but the order parameter now models the final heavy-atom to heavy-atom bond for each sidechain (see Methods).

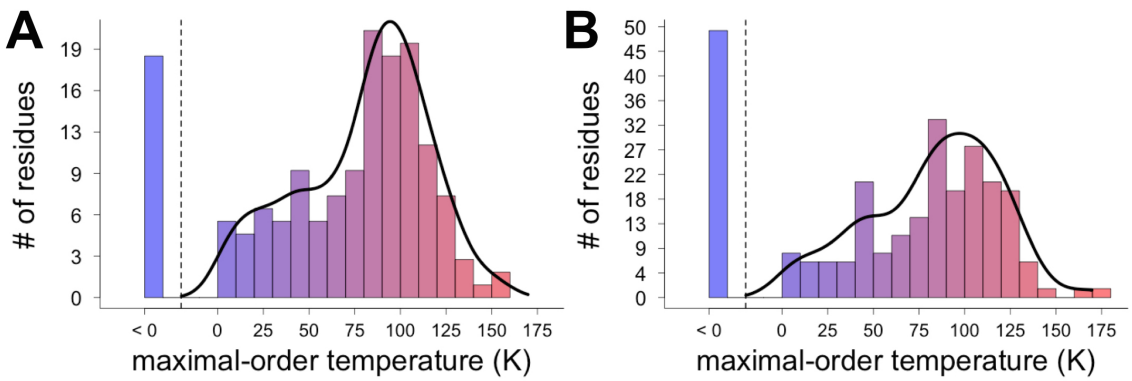

Figure 6 - Figure Supplement 5: Different residues extrapolate to different maximal-order temperatures. Fit lines for temperature points at 240 K and above were used to extrapolate to the maximal-order temperature, at which 1 - S^2 = 0. **(A)** Order parameter modeling the bond most closely associated with the χ1 dihedral angle. **(B)** Order parameter modeling the final heavy-atom to heavy-atom bond for each sidechain.

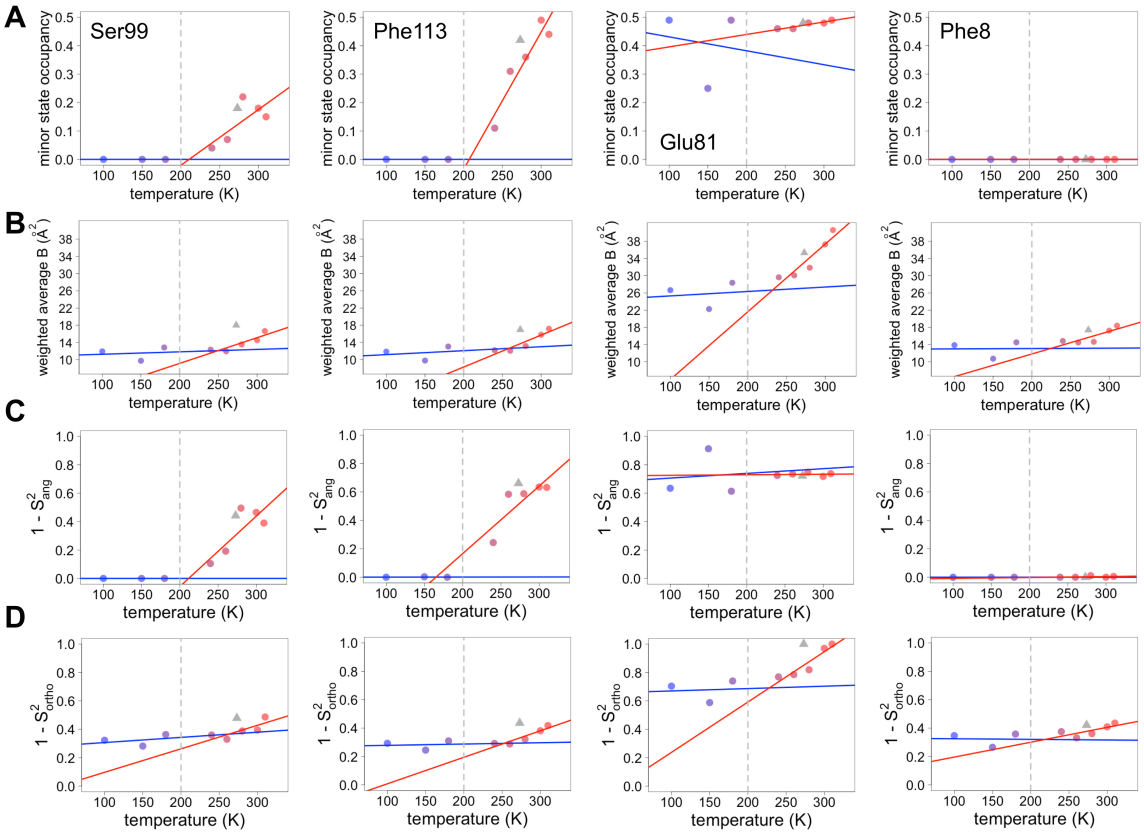

Figure 6 - Figure Supplement 6: Both harmonic and non-harmonic flexibility contribute to changes in order parameters with temperature. (A-D) Contributions to χ1 order parameter vs. temperature for four representative residues in CypA. Ser99 and Phe113 are in the active-site network, Glu81 is surface-exposed and adopts alternative conformations at all temperatures (**Figure 4**), and Phe8 is buried in the protein core and is single-rotamer at all temperatures. Similar conformations within the same rotameric well were grouped together for this analysis. **(A)** Occupancy of minor alternative conformations. **(B)** Intra-residue heavy-atom-average B-factor. **(C)** Complement of the S^2_{ang} component of the χ1 order parameter, which uses occupancy-weighted angles between bond vectors across alternative conformations. **(D)** Complement of the S^2_{ortho} component of the χ1 order parameter, which uses occupancy-weighted B-factors. Placement of XFEL points and coloring as in **Figure 6A**.

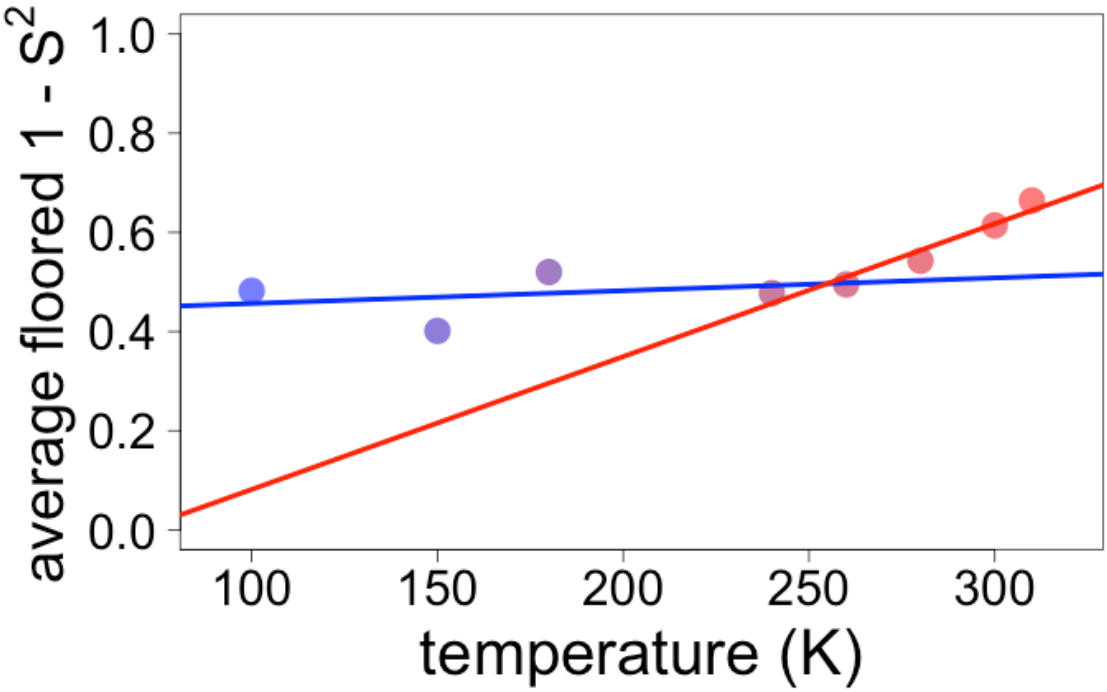

Figure 6 - Figure Supplement 7: Globally averaged disorder exhibits an apparent transition near 250 K. Points indicate observed values for the complement of sidechain order parameters, floored at 0 and then averaged over all residues in CypA, as in **Figure 6**. The blue and red lines represent fits to the ≤180 K and ≥240 K floored and averaged points, respectively. The fits to these globally averaged data suggest a transition at ~250 K, even though the underlying heterogeneity of the individual residue responses does not indicate there is a transition near this temperature.

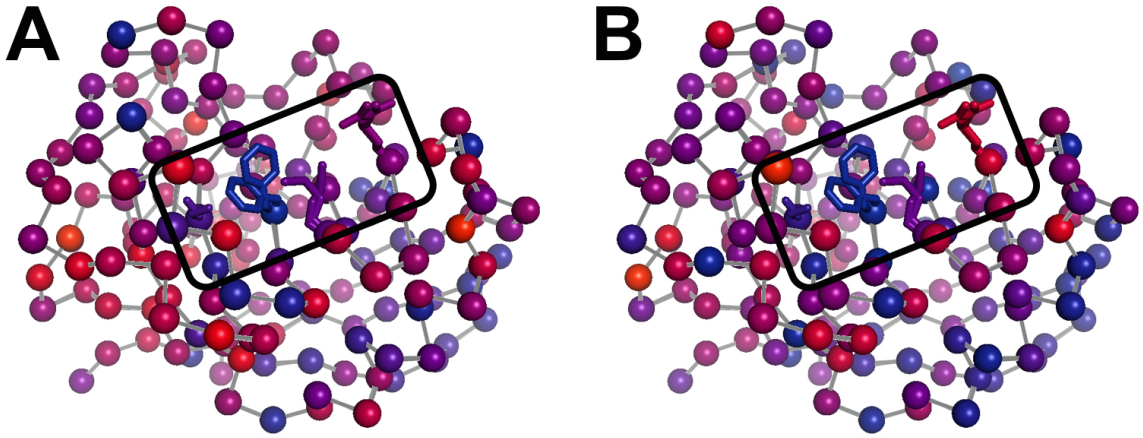

Figure 7: The temperature dependence of sidechain disorder is is nonhomogenously spatially distributed in CypA. Intersection temperatures from **(A)** χ1 order parameters as in **Figure 6B** or **(B)** sidechain terminus order parameters as in **Figure 6 – Figure Supplement 3 B** are mapped to the 1.2 Å room-temperature synchrotron model. Each residue is marked with a sphere colored based on its apparent transition temperature, from low (blue) to high (red). The active-site network is subdivided: Ser99 and Phe113 (left of boxed region) both transition at a low temperature regardless of order parameter bond vector, but Met61 and Arg55 transition at higher, different temperatures.

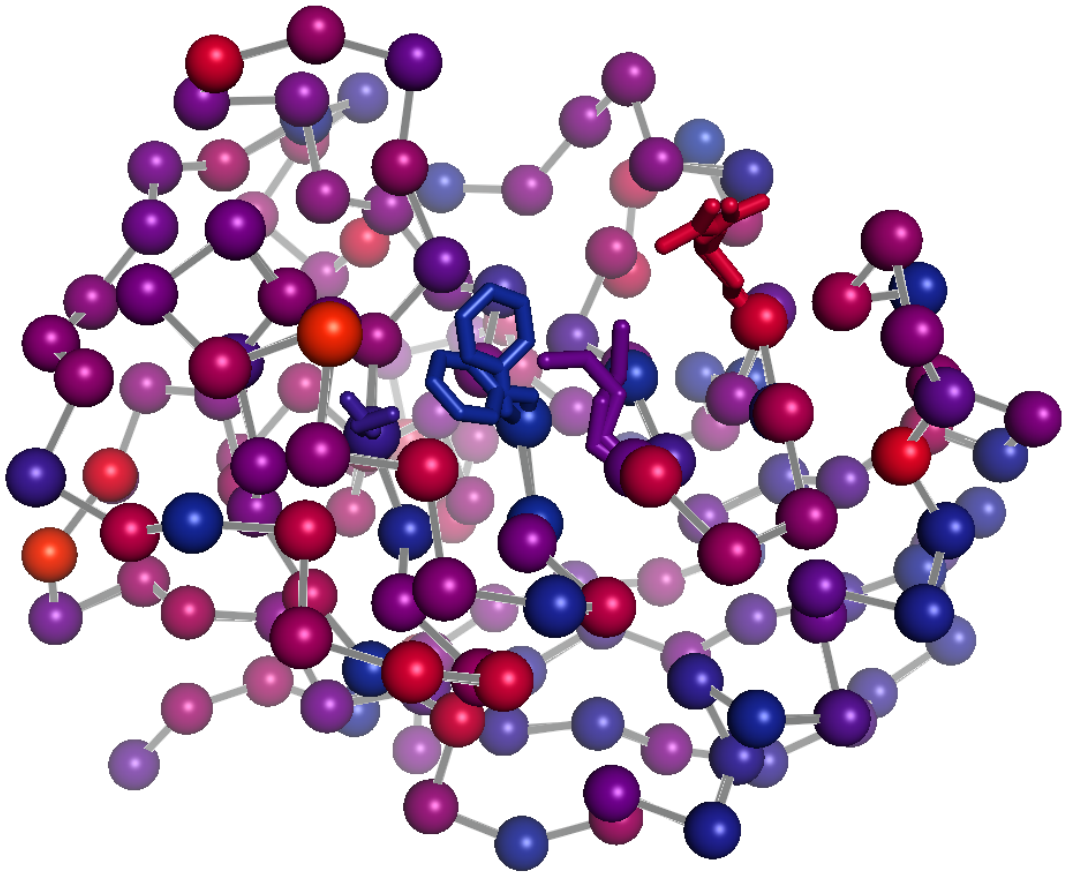

Movie 4: 360˚ rotation around **Figure 7B**.

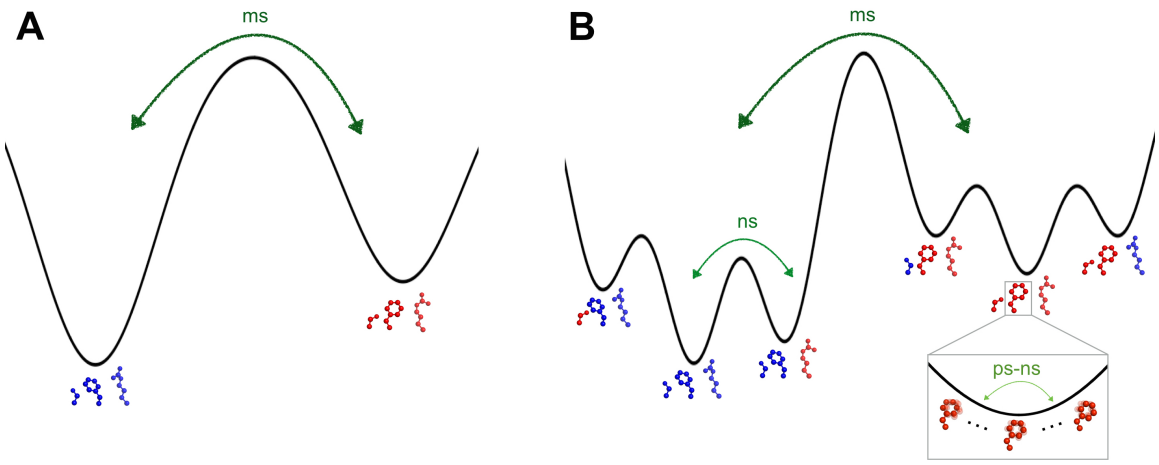

Figure 8: The dynamic active-site network of CypA has a complex energy landscape. (A) The previous simple model in which Ser99, Phe113, and Arg55 (Met61 omitted for clarity) interconvert from one macrostate (blue) to the other (red) completely collectively. NMR data suggest this process occurs on a millisecond timescale. **(B)** A more nuanced model in which network microstates are populated differently depending on the network macrostate, defined by the Phe113 rotameric state. In the left macrostate, Ser99 rotamer changes are disfavored because of steric overlaps with Phe113, but Arg55 rotamer changes are accommodated; the reverse is true (perhaps to a lesser extent) in the right macrostate. Within each microstate, rapid thermal motions occur (bottom right), and may alleviate some minor steric overlaps. Timescales are estimates consistent with NMR observables for CypA and other systems.